analytical chemistry

pubs.acs.org/ac Article

Recombination between ^{13}C and ^{2}H to Form Acetylide ($^{13}C_2{}^{2}H^-$) Probes Nanoscale Interactions in Lipid Bilayers via Dynamic Secondary Ion Mass Spectrometry: Cholesterol and GM_1 Clustering

Dashiel S. Grusky, Frank R. Moss, III, and Steven G. Boxer*

Cite This: *Anal. Chem.* 2022, 94, 9750−9757 Read Online

ACCESS | Metrics & More | Article Recommendations | Supporting Information

ABSTRACT: Although it is thought that there is lateral heterogeneity of lipid and protein components within biological membranes, probing this heterogeneity has proven challenging. The difficulty in such experiments is due to both the small length scale over which such heterogeneity can occur, and the significant perturbation resulting from fluorescent or spin labeling on the delicate interactions within bilayers. Atomic recombination during dynamic nanoscale secondary ion imaging mass spectrometry (NanoSIMS) is a non-perturbative method for examining nanoscale bilayer interactions. Atomic recombination is a variation on conventional NanoSIMS imaging, whereby an isotope on one molecule combines with a different isotope on another molecule during the ionization process, forming an isotopically enriched polyatomic ion in a distance-dependent manner. We show that the recombinant ion, $^{13}C_2{}^{2}H^-$, is formed in high yield from ^{13}C- and ^{2}H-labeled lipids. The low natural abundance of triply labeled acetylide also makes it an ideal ion to probe GM_1 clusters in model membranes and the effects of cholesterol on lipid−lipid interactions. We find evidence supporting the cholesterol condensation effect as well as the presence of nanoscale GM_1 clusters in model membranes.

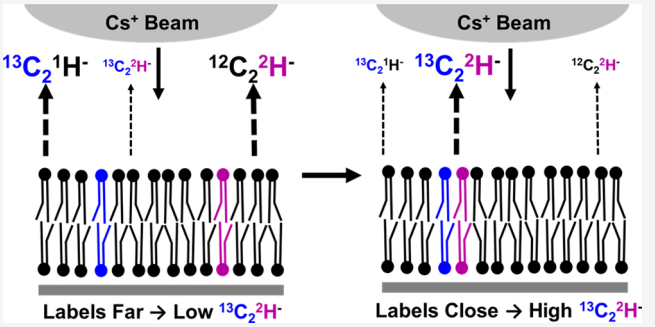

INTRODUCTION

Biological membranes are composed of a diverse collection of proteins and lipids. Some of the most studied mammalian lipids are glycerophospholipids, sphingolipids, and sterols. Cholesterol is of particular interest because it is thought to mediate the formation of nanoscale-ordered and -disordered domains composed of saturated lipids and unsaturated lipids, respectively.[1,2] This nanoscale separation has implications for biological functions such as signal transduction,[3] trafficking,[4] and viral binding.[5] Furthermore, cholesterol is thought to have a condensing effect on lipid bilayers, whereby the average area per lipid decreases as a function of increasing cholesterol concentration. This has been attributed to cholesterol having an ordering effect on lipid tail groups; however, much of the evidence for this condensing effect is limited to simulations[6−8] or compression of monolayers.[9−11] The glycolipid GM_1, found widely in brain tissue, has also been suggested to engage in nanoscale clustering,[12−14] with downstream effects on amyloid fibril formation[15,16] and growth factor function.[17,18]

It is challenging to study lipid clustering on a molecular length scale, and direct, non-perturbative experimental evidence for such clustering remains elusive. Many studies examine domains via detergent extraction,[19−21] fluorescence,[22−27] or single-particle tracking,[2,28,29] to name a few.[23,30,31] These methods all involve significant perturbations to the lipid system,[32,33] which makes it difficult to determine if the evidence for the domain existence and size is due to the colocalization of the natural components or the perturbations caused by the analytical method.[32−36] Additionally, there is evidence that nanodomains may be smaller than 10 nm, placing them well below the diffraction limit of conventional microscopy.[2] Even the most sophisticated super-resolution methods,[37,38] which require perturbative dye labeling,[33] are challenged by these dimensions, further complicating how such interactions are investigated. Therefore, if clustering on the nanometer scale is to be studied, novel analytical methods need to be developed.

Nanoscale secondary ion mass spectrometry (NanoSIMS) can probe the organization of bilayers on the nanometer scale using isotopically labeled lipids. The NanoSIMS 50L functions by rastering a freeze-dried bilayer sample with a Cs^+ primary ion beam. Sputtered secondary ions from the sample are then separated by a mass analyzer, allowing for up to seven unique

Received: March 27, 2022
Accepted: June 14, 2022
Published: June 27, 2022

https://doi.org/10.1021/acs.analchem.2c01336
Anal. Chem. 2022, 94, 9750−9757

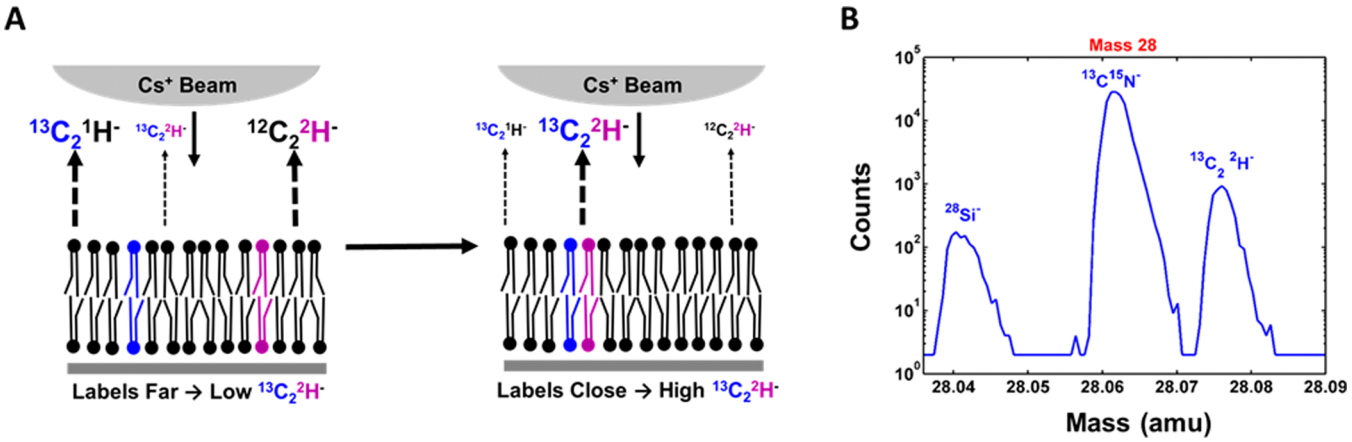

Figure 1. Recombination experiment scheme and acetylide mass scan. (A) Formation of the triply labeled acetylide ion ($^{13}C_2{}^2H^-$) depends on the average distance between ^{13}C and ^2H labels on different lipids in a supported lipid bilayer during Cs^+ bombardment (typical beam diameter is 50 nm, not to scale, and limiting the lateral resolution for conventional imaging). When the differently labeled lipids are closer together, more triply labeled acetylide is detected. In this figure and all subsequent figures, blue-colored lipids will correspond to ^{13}C-labeled lipids, while the purple lipids correspond to ^2H-labeled lipids. (B) Acetylide ion mass is well separated from any interfering isobars. Panel B is adapted from ref 42 (Moss, F. R.; Boxer, S. G. Atomic Recombination in Dynamic Secondary Ion Mass Spectrometry Probes Distance in Lipid Assemblies: A Nanometer Chemical Ruler. J. Am. Chem. Soc. 2016, 138 (51), 16737−16744).

masses to be detected simultaneously. The advantage of this technique is that it can provide compositional information, via the calculation of high-precision isotope ratios.[39−41] This can be done on length scales ranging from a few microns to as little as 1 nm using secondary ion recombination, discussed in detail in the following.[42] This makes NanoSIMS an appealing method to examine nanoscale organization. Furthermore, the isotopic labeling required to identify unique lipid species causes minimal perturbation to the delicate intermolecular interactions within a bilayer.

Our group has developed methods to examine the macroscale organization of lipid bilayer patches using the 50 nm lateral resolution (determined by the primary ion beam diameter) of the NanoSIMS.[41,43] However, we recently demonstrated that atomic recombination can be applied to examine membrane organization below this lateral resolution limit.[42] This is particularly useful as colocalization of membrane components could take place on the nm length scale.[44,45] Atomic recombination is observed following sample ionization by the primary cesium beam. For example, if the sample is labeled with ^{13}C and ^{15}N on different molecules, then collisional sputtering of the sample results in the formation of $^{13}C^{15}N^-$,[46] possibly through the gas-phase reaction of unstable species. Although the mechanism behind the process of recombination is not fully understood, it has been established that recombination depends not only on the chemical connectivity of labels (i.e., what the labels are covalently attached to) but also on the average distance between the two differently labeled molecules.[42,46,47] Critically, this distance dependence has been shown to be sensitive within 1−3 nm. This makes recombination a promising method to examine nanoscale colocalization of lipids within bilayers.

Here, recombination between ^{13}C and ^2H to form a triply labeled acetylide ion, $^{13}C_2{}^2H^-$, is applied to examine nanoscale lipid interactions. Figure 1A shows schematically that as the average distance between a ^{13}C-labeled lipid and a ^2H-labeled lipid decreases, the formation of triply labeled acetylide is expected to increase. While both recombinant $^{13}C_2{}^2H^-$ and $^{13}C^{15}N^-$ are well separated from any interfering ions (Figure 1B), the advantage of recombinant $^{13}C_2{}^2H^-$ is that it has much lower natural abundance (20 ppb) than $^{13}C^{15}N^-$ (44,000 ppb). This means that recombinant acetylide has an improved signal-to-background ratio. Furthermore, because there are more labeling sites for ^2H relative to ^{15}N on lipids, more ^2H labels can be incorporated into a lipid of interest, improving sensitivity. Additionally, ^2H labeling opens the possibility of labeling lipid tail groups, where interactions critical to lateral heterogeneity are presumed to take place. Finally, although the acetylide ion is a triatomic species, it forms in higher yield compared to other $C_xH_y^-$ ions. Given these advantages, ^{13}C and ^2H recombination to form acetylide should be an ideal method to investigate the subtle effects of cholesterol on lipid organization as well as interactions between lipids that are present in lower concentrations in biological membranes, such as the important glycolipid GM_1. Using the acetylide ion, the condensing effect of cholesterol is demonstrated via recombination. Additionally, ^{13}C and ^2H recombination to form acetylide is used to demonstrate nanoscale GM_1 clustering in model membranes. Finally, nanoscale interaction between saturated lipids is demonstrated in brain lipid extracts.

MATERIALS AND METHODS

Unlabeled phospholipids, cholesterol (CHOL), $^2H_{31}$−POPC (1-palmitoyl-2-oleoyl-*sn*-glycero-3-phosphocholine), and $^2H_{70}$−DSPC (1,2-distearoyl-*sn*-glycero-3-phosphocholine) were purchased from Avanti Polar Lipids. Unlabeled GM_1 was purchased from Biosynth-Carbosynth. Texas Red 1,2-dihexadecanoyl-*sn*-glycero-3-phosphoethanolamine (TR-DHPE) was purchased from Thermo Fisher Scientific. All solvents were purchased from Fisher. Four-inch <100> p-type silicon wafers with a 9.5 nm SiO_2 layer were purchased from Silicon Quest International, and were diced to 5 × 5 mm to fit in the NanoSIMS sample holder. This thickness of SiO_2 has previously been found to provide a compromise between charge dissipation during the NanoSIMS measurements and bilayer stability.[43,48] A grid (25, 50 or 100 μm^2) patterned with chrome (5 nm height and 5 μm width) was imprinted on the substrates via photolithography to facilitate correlative imaging.

Labeled Lipid Synthesis. $^{13}C_{18}$−POPC, $^{13}C_{18}$−DSPC, $^{13}C_{18}$−GM_1, and $^2H_{35}$−GM_1 were synthesized by adapting

https://doi.org/10.1021/acs.analchem.2c01336
Anal. Chem. 2022, 94, 9750−9757

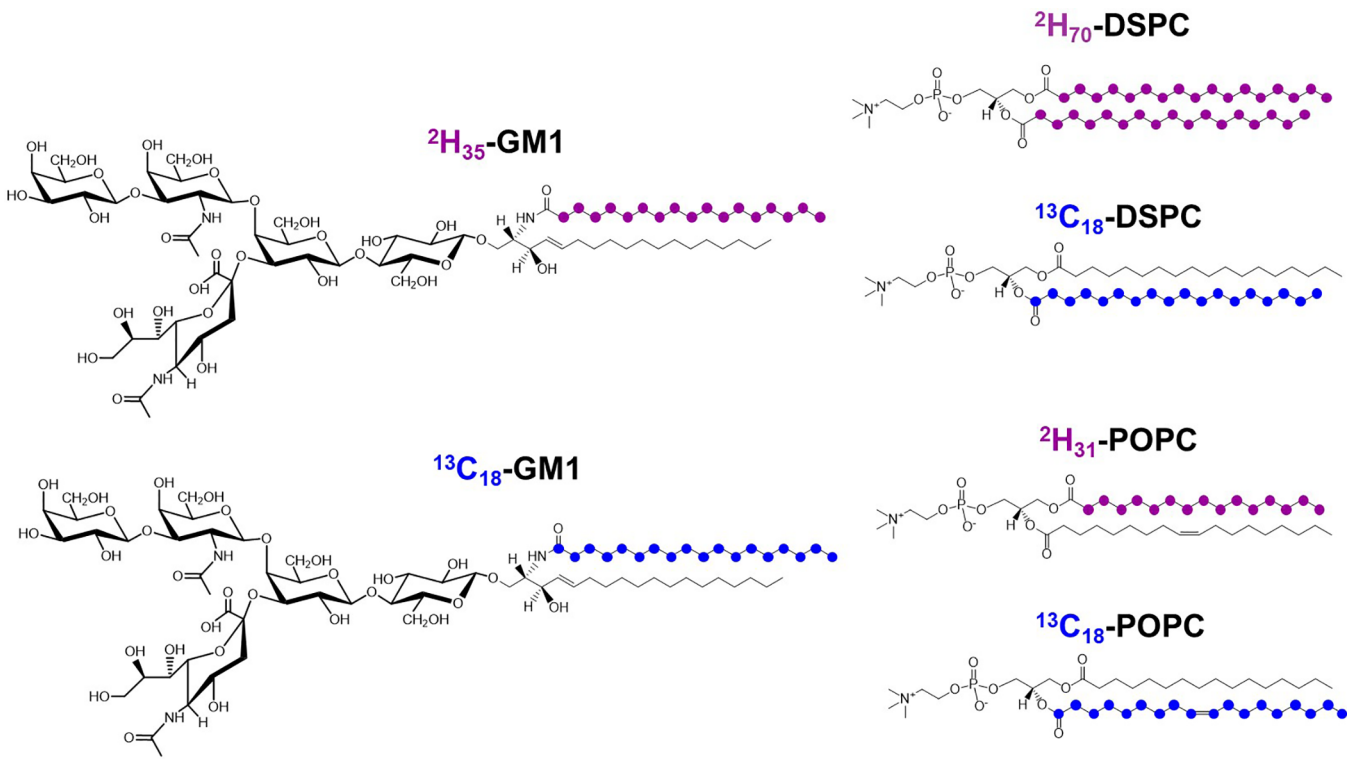

Figure 2. Labeled lipids. The isotopically labeled lipids used in this study are shown above. Colored circles represent the location of ^{13}C or ^{2}H labels. Synthetic protocols are further described in Sections 1 and 2 of the Supporting Information.

previously described methods[41,49,50] to attach isotopically labeled fatty acids to the appropriate lysolipid. Detailed synthetic protocols and methods can be found in Sections 1 and 2 (and in Figures S1 and S2) of the Supporting Information. Structures for these as well as all other labeled lipids used in this study are shown in Figure 2.

NanoSIMS Sample Preparation. Supported lipid bilayer (SLB) patches were formed via fusion of giant unilamellar vesicles (GUVs) to oxidized silicon substrates. GUVs were produced by the method of gentle hydration.[51,52] Briefly, lipid mixtures containing ^{13}C- and ^{2}H-labeled lipids, as well as 0.1 mol percent TR-DHPE, were mixed from stock solutions before being dried down under a stream of argon and then further desiccated for at least 4 h under house vacuum. The concentrations of lipid stock solutions were regularly calibrated via electrospray ionization mass spectroscopy (ESI-MS) with lipid standards. The mixtures were then rehydrated in a submicron-filtered 500 mM sucrose solution and heated to 65 °C, above the melting point of the high melting point lipid (DSPC 54 °C) for 15 h. Silicon substrates were plasma cleaned for 10 min. Following plasma cleaning, GUVs were cooled to room temperature and deposited onto silicon substrates in phosphate buffer (240 mM NaCl, 10 mM NaH_2PO_4 at pH 7.4). The deposition of GUVs was monitored via fluorescence microscopy using trace amounts (0.1 mol percent) of TR-DHPE, until 30−40% of the substrate was covered in SLB patches. The substrates and bilayer were then washed extensively with ultrapure water, flash-frozen in liquid nitrogen, and subjected to low pressure for 12 h to sublime vitreous ice. This procedure has previously been shown to preserve bilayer morphology at high resolution.[43] The substrates were then examined by fluorescence microscopy. The chrome pattern on the substrate further assists in finding regions of the substrate, where individual bilayers were formed from the rupture of single GUVs.

Asymmetric bilayers were prepared via Langmuir−Blodgett (LB)−Langmuir−Schaffer (LS) methods. First, LB monolayers were compressed and deposited onto diced silicon wafers using a KSV NIMA KN 2002 (Biolin Scientific, Stockholm, Sweden) Langmuir trough (273 cm^2). A Whatman filter paper was used as a Wilhelmy plate to monitor surface pressure. The lipid mixture for the lower leaflet dissolved in chloroform was spread on water (>18 MΩ from Milli-Q system) placed within the clean trough. The chloroform was left to evaporate for 10 min before compressing the barriers at 10 mm/min until the surface pressure reached 32 mN/m. Plasma-cleaned NanoSIMS substrates were glued with E6000 adhesive (Eclectic Products) to a glass slide. The glass slide and attached substrate were then pulled through the air−water interface at a rate of 1 mm/min while the surface pressure was maintained at 32 mN/m, creating a monolayer on the surface (such monolayers are stable in air).[42] Then, a new monolayer with the upper leaflet lipid mixture was formed on the trough. The substrate with the deposited lower leaflet monolayer was then removed from the glass slide before the glue dried and passed through the air−water interface perpendicular to the surface to deposit the upper leaflet. Because SLBs are not stable in air,[53] the substrate was removed such that a drop of water remained on the surface with the asymmetric bilayer. The substrate was then rapidly flash-frozen in liquid nitrogen and subjected to low pressure as previously described.

NanoSIMS Analysis. Analysis was performed on the Cameca NanoSIMS 50L at Stanford University. Images were collected at room temperature with a 2 pA $^{133}Cs^{+}$ primary beam. Ten 25 μm × 25 μm scans of 256 × 256 pixels were collected (enough to remove all the deposited lipid from the

https://doi.org/10.1021/acs.analchem.2c01336
Anal. Chem. 2022, 94, 9750−9757

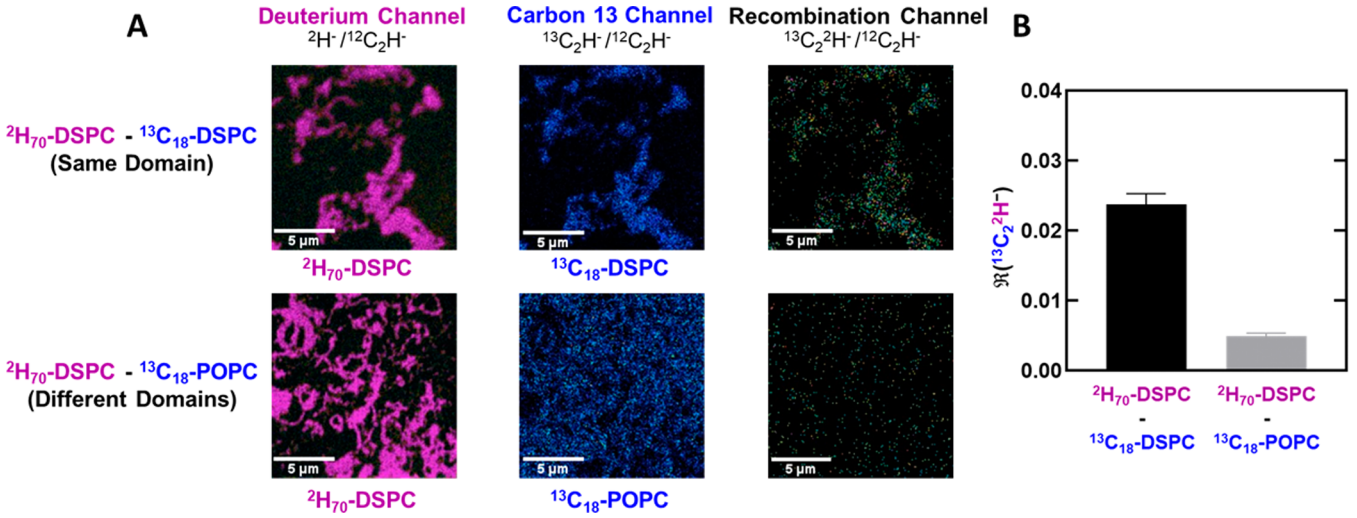

Figure 3. Recombination in macroscopic domains. (A) NanoSIMS images of two bilayer patches with isotopically labeled lipids placed in the same or different macroscopic domains. Each channel displays the standardized signal from a bilayer patch for the indicated ion. Sample compositions are $^{13}C_{18}$–DSPC:$^{2}H_{70}$–DSPC:POPC 25:25:50 (same domain) and $^{2}H_{70}$–DSPC:DSPC:$^{13}C_{18}$–POPC:POPC 25:25:25:25 (different domains). The upper row displays a bilayer where the ^{2}H-labeled lipid ($^{2}H_{70}$–DSPC) and the ^{13}C-labeled lipid ($^{13}C_{18}$–DSPC) both localize to the DSPC-rich gel domains. High recombination is observed in these domains because the ^{13}C and ^{2}H labels are close. The lower row of NanoSIMS images displays the second bilayer where the ^{2}H-labeled lipid ($^{2}H_{70}$–DSPC) localizes to the gel domains and ^{13}C-labeled lipid ($^{13}C_{18}$–POPC) localizes to the disordered domains. Less recombination is observed as the ^{13}C and ^{2}H labels are farther apart on average. (B) Quantification of recombination between ^{13}C and ^{2}H to form $^{13}C_2{}^{2}H^{-}$ in the gel domains. Samples where labeled lipids localize to the same ($^{2}H_{70}$–DSPC–$^{13}C_{18}$–DSPC) or different ($^{2}H_{70}$–DSPC–$^{13}C_{18}$–POPC) domains are compared. The recombination ratio $\Re(^{13}C_2{}^{2}H^{-}) \equiv {}^{13}C_2{}^{2}H^{-}/(^{13}C_2{}^{2}H^{-} + {}^{13}C_2{}^{1}H^{-} + {}^{12}C_2{}^{2}H^{-})$ is higher when both labeled lipids are in the DSPC-rich gel domains and are therefore closer together on average. Error bars in this and all subsequent figures display the 95% confidence interval. Seven bilayer patches were examined for each sample.

surface) with a dwell time of 1 ms/pixel. The ion detectors were set to $^{2}H^{-}$, $^{12}C^{-}$, $^{13}C^{-}$, $^{12}C_2{}^{1}H^{-}$, $^{12}C_2{}^{2}H^{-}$, $^{13}C_2{}^{1}H^{-}$, and $^{13}C_2{}^{2}H^{-}$. Secondary electron images were collected simultaneously. Standard samples were regularly analyzed to ensure that isotope ratios were reproducible from day to day and session to session. Because all samples were freeze-dried and analyses were carried out under ultrahigh vacuum, there should be minimal water and oxygen in the sample.

Data Analysis. Images were analyzed using ImageJ (National Institutes of Health, USA) with the OpenMIMS plugin (National Resource for Mass Spectrometry, Harvard University USA). Planes were summed and regions of interest were manually selected to exclude debris on the sample. Total counts within each region of interest were determined via the "Tomography" tab. These counts were then used to determine the ratio of interest, $\Re(^{13}C_2{}^{2}H^{-}) \equiv {}^{13}C_2{}^{2}H^{-}/(^{13}C_2{}^{2}H^{-} + {}^{13}C_2{}^{1}H^{-} + {}^{12}C_2{}^{2}H^{-})$, to control for the size of the analyzed bilayer (formed from the rupture of a single GUV) and for variations in ionization efficiency.

RESULTS AND DISCUSSION

Recombination to Form Acetylide is Distance-Dependent. To demonstrate that the formation of triply labeled acetylide depends on the average distance between ^{13}C and ^{2}H labels on different molecules, GUV patches (formed from the rupture of individual GUVs) with microscale coexisting phases were prepared, as was done in earlier work with ^{13}C and ^{15}N recombination to form $^{13}C^{15}N^{-}$.[42] A mixture of 50:50 POPC:DSPC was examined. This mixture has microscale phase separation between DSPC and POPC that is visible by conventional NanoSIMS imaging (50 nm lateral resolution). Furthermore, mixtures of these lipids are well studied in GUVs.[44,45] In this composition, the saturated lipids cluster together into gel domains, while the unsaturated lipids cluster into disordered domains. The effect of average distance between ^{13}C and ^{2}H labels was examined by comparing recombination in bilayers containing $^{13}C_{18}$–DSPC and $^{2}H_{70}$–DSPC to bilayers containing $^{13}C_{18}$–POPC and $^{2}H_{70}$–DSPC. If the formation of $^{13}C_2{}^{2}H^{-}$ is a distance-dependent process, then recombination between ^{13}C and ^{2}H to form $^{13}C_2{}^{2}H^{-}$ should be high in bilayers where both the ^{13}C and ^{2}H lipids localize to the gel domain. Conversely, the formation of $^{13}C_2{}^{2}H^{-}$ should be low in bilayers, where the ^{13}C-labeled lipid localizes to the disordered domain and the ^{2}H-labeled lipid localizes to the gel domain. As can be seen in Figure 3A, when both labels are in the same domains ($^{2}H_{70}$–DSPC–$^{13}C_{18}$–DSPC) there are high standardized counts (ratio shown above the images in Figure 3A) of the recombinant ion within the DSPC-rich domains. When the labels are placed on lipids that localize to different domains ($^{2}H_{70}$–DSPC–$^{13}C_{18}$–POPC), such a high signal is not seen visually. Quantification of the recombination ratio, $\Re(^{13}C_2{}^{2}H^{-}) \equiv {}^{13}C_2{}^{2}H^{-}/(^{13}C_2{}^{2}H^{-} + {}^{13}C_2{}^{1}H^{-} + {}^{12}C_2{}^{2}H^{-})$, within the gel domains of both samples is shown in Figure 3B. This quantification recapitulates the visual results from Figure 3A. Only in bilayers where the ^{13}C- and ^{2}H-labeled lipids colocalize to the same region, and are therefore closer, is high $\Re(^{13}C_2{}^{2}H^{-})$ seen. Having established that recombination to form $^{13}C_2{}^{2}H^{-}$ is distance-dependent, much like $^{13}C^{15}N^{-}$,[42] atomic recombination was then used to examine the effects of cholesterol on nanoscale lipid–lipid interactions.

Effects of Cholesterol on Lipid–Lipid Interactions. The advantage of atomic recombination is that it circumvents the lateral resolution limit of the NanoSIMS[42] (approximately 50 nm). This makes it possible to use $^{13}C_2{}^{2}H^{-}$ formation to probe subtle effects of cholesterol in mixtures with nanoscale, rather than microscale, phase separation or clustering. To

https://doi.org/10.1021/acs.analchem.2c01336
Anal. Chem. 2022, 94, 9750–9757

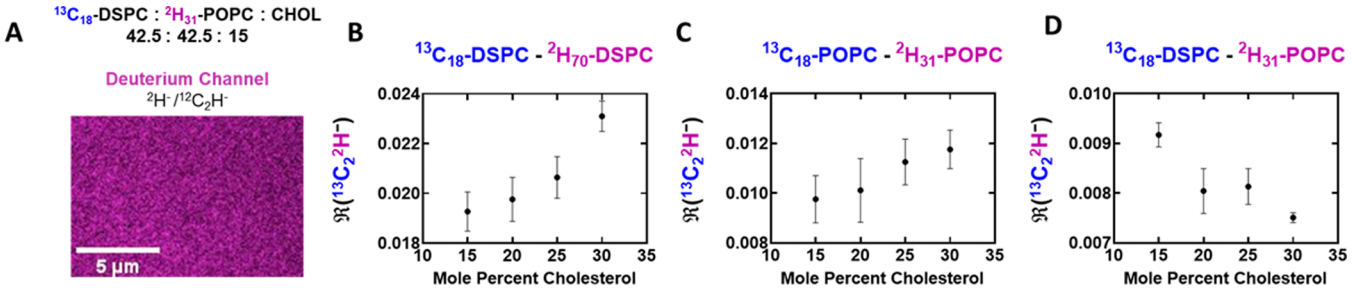

Figure 4. Effect of cholesterol on lipid−lipid interactions. (A) Representative image of the standardized deuterium signal in a bilayer with a composition $^{13}C_{18}$−DSPC:$^{2}H_{31}$−POPC:CHOL 42.5:42.5:15. No resolvable heterogeneity can be seen. (B−D) $\Re(^{13}C_{2}{}^{2}H^{-})$ as a function of cholesterol. For each plot, the labeled lipids contained in the bilayer are denoted in the title. (B,C) Increasing $\Re(^{13}C_{2}{}^{2}H^{-})$ with cholesterol concentration when labels are placed within the same nanoscale domain. (D) Decreasing $\Re(^{13}C_{2}{}^{2}H^{-})$ is seen as a function of cholesterol concentration when labels are placed in different nanoscale domains. See Table S1 for detailed compositional information. For each data point, a minimum of 10 individual bilayer patches was examined.

probe the effects of cholesterol on the average distance between lipids, bilayers composed of POPC/DSPC/CHOL were studied, as this mixture exhibits nanoscale heterogeneity at certain compositions.[44,45] As can be seen in Figure 4A, conventional NanoSIMS imaging cannot resolve any heterogeneity in the displayed bilayer, in contrast to the bilayers shown in Figure 3A. However, atomic recombination can still distinguish between samples, where labeled lipids are placed in the same versus different nanoscale clusters (Figure S3).

To examine the effects of cholesterol on lipid−lipid interactions, bilayers containing 15, 20, 25, and 30 mol percent cholesterol with a constant 1:1 POPC:DSPC lipid ratio were prepared. These samples contained ^{13}C- and ^{2}H-labeled lipids in either the same ordered ($^{13}C_{18}$−DSPC and $^{2}H_{70}$−DSPC), disordered ($^{13}C_{18}$−POPC and $^{2}H_{31}$−POPC) or different ($^{13}C_{18}$−DSPC and $^{2}H_{31}$−POPC) nanoscale domains. The effects of cholesterol on lipids within and between domains were systematically probed by tracking how $\Re(^{13}C_{2}{}^{2}H^{-})$ varies with cholesterol concentration. Detailed compositional information can be found in Table S1 and Figure S4. To maximize $\Re(^{13}C_{2}{}^{2}H^{-})$, a 1:1 mol ratio of ^{13}C-labeled lipid to ^{2}H-labeled lipid was used (Figure S6).

The effects of increasing cholesterol concentration on $\Re(^{13}C_{2}{}^{2}H^{-})$ can be seen in Figure 4B−D. As the cholesterol concentration is increased, there is a statistically significant increase in $\Re(^{13}C_{2}{}^{2}H^{-})$ for bilayers containing $^{13}C_{18}$−DSPC and $^{2}H_{70}$−DSPC, as well as bilayers containing $^{13}C_{18}$−POPC and $^{2}H_{31}$−POPC. Conversely, there is a significant decrease in $\Re(^{13}C_{2}{}^{2}H^{-})$ for bilayers containing $^{13}C_{18}$−DSPC and $^{2}H_{31}$−POPC. It can therefore be concluded that for the first two cases ($^{13}C_{18}$−DSPC−$^{2}H_{70}$−DSPC and $^{13}C_{18}$−POPC−$^{2}H_{31}$−POPC), the average distance between the ^{13}C- and ^{2}H-labeled lipids decreases as the cholesterol concentration increases. For the third case ($^{13}C_{18}$−DSPC−$^{2}H_{31}$−POPC), the average distance between the ^{13}C- and ^{2}H-labeled lipids increases as the cholesterol concentration increases.

The trend observed for $^{13}C_{18}$−DSPC−$^{2}H_{70}$−DSPC and $^{13}C_{18}$−POPC−$^{2}H_{31}$−POPC bilayers can be attributed to the cholesterol condensation effect, which should closely pack lipids within a nanoscale domain.[7,54−56] Prior simulations suggest that this packing effect outweighs the dilution of lipids due to the addition of cholesterol,[7] a finding that our data supports. This close packing decreases the average distance between ^{13}C- and ^{2}H-labeled lipids resulting in a larger $\Re(^{13}C_{2}{}^{2}H^{-})$. Interestingly, the measured $\Re(^{13}C_{2}{}^{2}H^{-})$ in $^{13}C_{18}$−DSPC and $^{2}H_{70}$−DSPC containing bilayers also decreases when transitioning from the macroscale gel phase (Figure 3B) to the nanoscale gel plus L_o phase (Figure 4B). This result means that cholesterol initially increases average distances between lipids within the same domain during the gel to L_o phase transition. The decrease in $\Re(^{13}C_{2}{}^{2}H^{-})$ upon transition likely results from a combination of the change in the domain size and the decreased lipid order in the L_o phase relative to the gel phase.[44]

$\Re(^{13}C_{2}{}^{2}H^{-})$ measured in bilayers containing $^{13}C_{18}$−DSPC and $^{2}H_{31}$−POPC displays the opposite trend. As the cholesterol concentration is increased, $\Re(^{13}C_{2}{}^{2}H^{-})$ decreases. This corresponds to an increase in the average distance between the ^{13}C- and ^{2}H-labeled lipids. This could be due to cholesterol localizing at domain interfaces, as has been suggested by simulations.[56−58] Interfacial partitioning may also provide an explanation for why cholesterol does not dilute the labeled lipids in ordered domains as its concentration increases (if this were a dominating factor, $\Re(^{13}C_{2}{}^{2}H^{-})$ would decrease in bilayers containing $^{13}C_{18}$−DSPC and $^{2}H_{70}$−DSPC as the cholesterol concentration increases). Furthermore, these trends in average distances cannot be entirely explained via analysis of domain composition using the phase diagram (Figure S4). According to the ternary phase diagram, as the cholesterol concentration increases there should be a corresponding increase in bilayer homogeneity as the phases become more similar in composition, and the fraction of the L_o phase increases. This is contrary to the data presented in Figure 4, which suggests greater average separation between DSPC and POPC than is expected based only on compositions of phases, indicating that lipid packing is changing between the different samples. This effect is modeled and further discussed in Figure S5 and Section 6 of the Supporting Information.

There are, however, potential effects due to the labeling strategy used, which may influence the observed $^{13}C_{18}$−DSPC−$^{2}H_{31}$−POPC $\Re(^{13}C_{2}{}^{2}H^{-})$ trend. In particular, the decreasing label concentration used for these mixtures may increase the average distance between labeled lipids, decreasing $\Re(^{13}C_{2}{}^{2}H^{-})$ (see Figures S7 and S8, Table S1, and the discussion in Section 8 in the Supporting Information).

GM_1 Clustering in Model Membranes. Previous work, largely simulations,[12,13] suggests that GM_1 can engage in nanoscale or macroscale clustering.[16,59] A truly non-perturbative confirmation of such clustering would help further understanding membrane interactions as well as protein−lipid interactions, as GM_1 clustering may have downstream

https://doi.org/10.1021/acs.analchem.2c01336
Anal. Chem. 2022, 94, 9750−9757

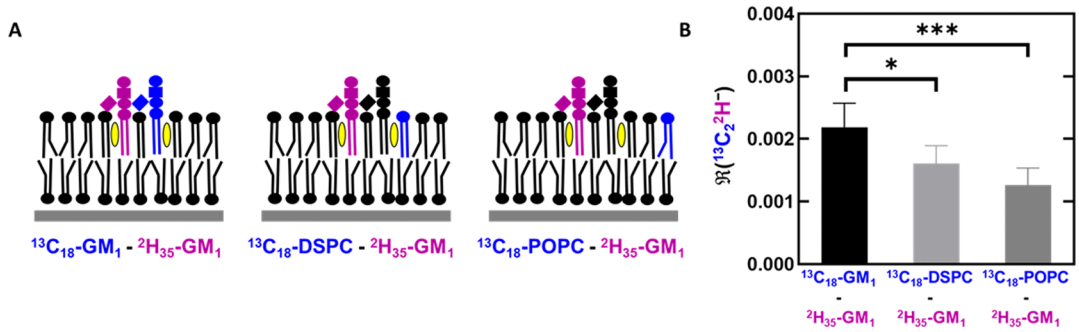

Figure 5. GM$_1$–lipid recombination. (A) Design of asymmetric bilayers containing isotopically labeled lipids in the upper leaflet for recombination. Lipids with a kinked chain represent POPC, lipids with straight chains represent DSPC, lipids with glycosylation are GM$_1$, and yellow ovals represent cholesterol. (B) Recombination between labeled lipids within asymmetric bilayers. All asymmetric bilayers were prepared with a pure POPC lower leaflet and upper leaflet composed of POPC:DSPC:GM$_1$:CHOL 48.75:16.25:10:25. For each sample, 10 mol % of labeled lipid (5 mol % $^{13}C_{18}$–GM$_1$, $^{13}C_{18}$–POPC or $^{13}C_{18}$–DSPC and 5 mol % $^{2}H_{35}$–GM$_1$) replaced the respective neutral lipid(s). Twenty independent bilayers were examined for each sample. $\Re(^{13}C_2{}^2H^-)$ in bilayers containing $^{2}H_{35}$–GM$_1$ and $^{13}C_{18}$–GM$_1$ is significantly different from $\Re(^{13}C_2{}^2H^-)$ in bilayers containing $^{2}H_{35}$–GM$_1$ and $^{13}C_{18}$–POPC or $^{13}C_{18}$–DSPC. * and *** represent significant differences with $p \leq 0.05$ and $p \leq 0.001$, respectively.

implications for amyloid fibril formation[60,61] and growth factor function.[62,63] Atomic recombination was further applied to probe this clustering.

Because GM$_1$ is present at low concentration in the plasma membrane of neurons, the extent of labeling necessary to identify nanoscale clustering was investigated. Figure S3 shows that recombination to form acetylide can detect nanoscale separation between saturated and unsaturated lipids using as little as 4 mol percent isotopically labeled lipid (2 mol percent of ^{13}C-labeled lipid and 2 mol percent ^{2}H-labeled lipid). Atomic recombination is therefore a plausible method for investigating nanoscale heterogeneity of components present in low concentrations, such as GM$_1$.

To examine whether GM$_1$ engages in local clustering, isotopically labeled GM$_1$ was synthesized as shown in Figure S2. This enables $\Re(^{13}C_2{}^2H^-)$ in bilayers containing $^{13}C_{18}$–GM$_1$ and $^{2}H_{35}$–GM$_1$ to be compared to $\Re(^{13}C_2{}^2H^-)$ in bilayers containing $^{2}H_{35}$–GM$_1$ and either $^{13}C_{18}$–POPC or $^{13}C_{18}$–DSPC. Previous work has suggested that GM$_1$ may localize to the upper leaflet in SLBs.[64] Therefore, in SLBs formed from GUV rupture, the average distance between $^{13}C_{18}$- and $^{2}H_{35}$–GM$_1$ may be artificially lower due to these lipids preferentially localizing to the upper leaflet. This in turn would lead to artificially higher $\Re(^{13}C_2{}^2H^-)$ relative to samples containing $^{13}C_{18}$–POPC or $^{13}C_{18}$–DSPC, as neither of these lipids localize to a particular leaflet. To avoid this, asymmetric bilayers were formed via LB–LS methods. A lower leaflet of POPC was deposited as a monolayer onto a patterned silicon substrate, after which it was plunged through a second monolayer containing $^{2}H_{35}$–GM$_1$, and either $^{13}C_{18}$–GM$_1$, $^{13}C_{18}$–POPC, or $^{13}C_{18}$–DSPC, before being rapidly freeze-dried. All lipid mixtures were compressed to 32 mN/m (approximately 60 A^2 for each molecule). The resulting bilayers have asymmetric leaflets as shown schematically in Figure 5A, with isotopically labeled lipids in only the upper leaflet.

The measured $\Re(^{13}C_2{}^2H^-)$ for bilayers with each labeled lipid pair ($^{2}H_{35}$–GM$_1$–$^{13}C_{18}$–GM$_1$, $^{2}H_{35}$–GM$_1$–$^{13}C_{18}$–DSPC, and $^{2}H_{35}$–GM$_1$–$^{13}C_{18}$–POPC) is shown in Figure 5B. The displayed ratios demonstrate highest $\Re(^{13}C_2{}^2H^-)$ in bilayers containing $^{2}H_{35}$–GM$_1$ and $^{13}C_{18}$–GM$_1$. $\Re(^{13}C_2{}^2H^-)$ in bilayers containing $^{2}H_{35}$–GM$_1$ and either $^{13}C_{18}$–DSPC or $^{13}C_{18}$–POPC is significantly lower. Bilayers containing $^{2}H_{35}$–GM$_1$ and $^{13}C_{18}$–DSPC do not display a significant difference in $\Re(^{13}C_2{}^2H^-)$ relative to those containing $^{2}H_{35}$–GM$_1$ and $^{13}C_{18}$–POPC (p = 0.078). Therefore, there is not sufficient evidence to suggest a preference for GM$_1$ interactions between saturated or unsaturated lipids. It is possible that such a preference exists, given that saturated lipids may pack better with GM$_1$ relative to unsaturated lipids; however, within the limits of this experiment, there is no detectable difference. Prior simulations suggest that GM$_1$–GM$_1$ interactions are mediated by specific interactions between cholesterol and GM$_1$. This, in addition to hydrogen bonding between GM$_1$ headgroups, may mediate the formation of clusters.[12,61,65] The experiments described here provide direct and label-free evidence for GM$_1$ clustering, consistent with previous simulations.

Recombination in Lipid Extracts. While the model systems examined thus far contain three to four components, biological membranes are considerably more complex. Therefore, a more complex mixture was examined to test if greater lipid diversity abolishes the nanoscale heterogeneity demonstrated above. A first approximation for this diversity can be achieved using natural lipid extracts. Although commercially available extracts obviously do not recapitulate the effect that peripheral and transmembrane proteins have on bilayer organization, they at least serve as a model for a more complex system with a greater variety in terms of lipid headgroups and unsaturation levels. To probe heterogeneity in this complex mixture, 3 nmol of $^{13}C_{18}$–DSPC and $^{2}H_{70}$–DSPC (same nanoscale domain) or $^{13}C_{18}$–POPC and $^{2}H_{70}$–DSPC (different nanoscale domains) were mixed into brain lipid extracts (Figure 6A). $\Re(^{13}C_2{}^2H^-)$ was compared between bilayer patches using the two labeling schemes. If nanoscale separation between saturated and unsaturated lipids is present in this more complex bilayer, then $\Re(^{13}C_2{}^2H^-)$ should be greater in bilayers containing $^{13}C_{18}$–DSPC and $^{2}H_{70}$–DSPC. As can be seen in Figure 6B, the measured $\Re(^{13}C_2{}^2H^-)$ for bilayers containing $^{13}C_{18}$–DSPC and $^{2}H_{70}$–DSPC is significantly greater than that measured for bilayers containing $^{13}C_{18}$–POPC and $^{2}H_{70}$–DSPC. This demonstrates that the increased lipid diversity of a comparatively more biological system does not abolish nanoscale clustering of saturated lipids. It is

https://doi.org/10.1021/acs.analchem.2c01336
Anal. Chem. 2022, 94, 9750−9757

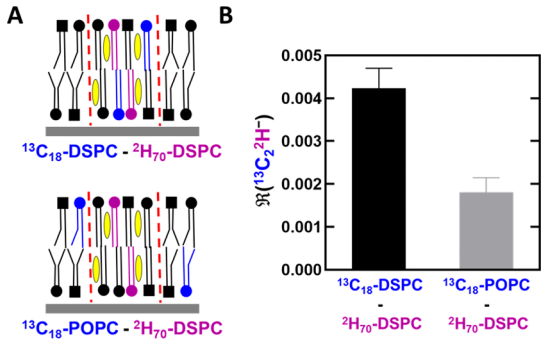

Figure 6. Recombination in brain lipid extracts. (A) Brain lipid extract SLBs containing $^{13}C_{18}$–DSPC and $^{2}H_{70}$–DSPC or $^{13}C_{18}$–POPC and $^{2}H_{70}$–DSPC. Isotopically labeled POPC and DSPC may be incorporated into different nanoscale domains in bilayers, highlighted schematically by the red dashed lines. 9 nmol of DSPC and 3 nmol POPC were added in total to each sample. Out of this, 3 nmol is ^{13}C lipid (either $^{13}C_{18}$–DSPC or $^{13}C_{18}$–POPC) and 3 nmol is $^{2}H_{70}$–DSPC (the added labeled and unlabeled lipid composes 20 percent of the total mass of the deposited bilayer). The remainder of the added mixture is natural abundance lipid. (B) Measured $\Re(^{13}C_2{}^2H^-)$ is higher in bilayers containing the saturated $^{13}C_{18}$- and $^{2}H_{70}$–DSPC lipids than those containing unsaturated $^{13}C_{18}$–POPC and saturated $^{2}H_{70}$–DSPC. Ten bilayer patches were examined for each sample.

possible that these interactions are mediated by cholesterol or result from favorable packing between saturated lipids relative to packing between saturated and unsaturated lipids.

CONCLUSIONS

The paucity of analytical methods to interrogate the lateral organization of biological membranes on the nanometer scale has proven to be a significant barrier to improving our understanding of these complex systems. This is largely due to the small length scale over which lipid–lipid interactions can occur and the significant perturbations conventional labeling strategies can have on the delicate and transient interactions between bilayer components. In this work, we build on previously established atomic recombination methods and take advantage of a previously unused ion ($^{13}C_2{}^2H^-$) with improved sensitivity. We apply this ion to examine fundamental questions regarding the effects of cholesterol on lipid interactions as well as the nanoscale interactions of GM_1. Recombination to form acetylide has also been leveraged to examine more complex systems that may serve as a better approximation of compositional heterogeneity present in a biological membrane.

There has been considerable debate over the past few decades over the role of cholesterol in lipid bilayers; much of the evidence for the condensation effect of cholesterol relies on simulation.[7,66] Recombination to form acetylide is a novel method for examining the subtle effects that cholesterol can have on bilayer organization. A particular advantage of atomic recombination is its non-perturbative nature, as it does not rely on fluorescent or spin labels,[30,67] commonly used for investigating membrane organization. Although a significant advantage of these conventional labels is that they can be present in low concentration and still attain a high signal, the work presented here demonstrates that atomic recombination is also quite sensitive. The large number of ^{13}C and ^{2}H labels that can be placed on lipids with relative ease leads to a reasonable signal even at relatively a low (a few mole percent) labeled lipid concentration.

Using this high sensitivity, we were able to demonstrate that there is evidence of preferential interaction between GM_1 lipids relative to other bilayer components, providing evidence for nanoscale GM_1 clustering. This emphasizes that recombination can be applied to study interactions between bilayer components that are present in low concentrations in biological membranes. Recombination methods can also be applied to more complex systems, such as lipid extracts, to detect nanoscale clustering. To obtain an even clearer picture of bilayer organization, atomic recombination could be used to examine more than lipid–lipid interactions such as protein–lipid or peptide–lipid interactions, and these applications are being pursued.

ASSOCIATED CONTENT

Supporting Information

The Supporting Information is available free of charge at https://pubs.acs.org/doi/10.1021/acs.analchem.2c01336.

Synthesis of $^{13}C_{18}$–POPC and $^{13}C_{18}$–DSPC; synthesis of $^{13}C_{18}$ NHS stearate and $^{2}H_{35}$ NHS stearate; synthesis of $^{13}C_{18}$–GM_1 and $^{2}H_{35}$–GM_1; examining lower limits of recombination; lipid compositions; optimization of the recombination signal; and concentration dependence of recombination (PDF)

AUTHOR INFORMATION

Corresponding Author

Steven G. Boxer − *Department of Chemistry, Stanford University, Stanford, California 94305, United States;* orcid.org/0000-0001-9167-4286; Email: sboxer@stanford.edu

Authors

Dashiel S. Grusky − *Department of Chemistry, Stanford University, Stanford, California 94305, United States;* orcid.org/0000-0002-0145-398X

Frank R. Moss, III − *Linac Coherent Light Source, SLAC National Accelerator Laboratory, Menlo Park, California 94025, United States;* orcid.org/0000-0002-6149-6447

Complete contact information is available at: https://pubs.acs.org/10.1021/acs.analchem.2c01336

Notes

The authors declare no competing financial interest.

ACKNOWLEDGMENTS

This work was supported by grants from NSF (MCB-1915727) and NIH (R35GM118044) to S.G.B. We thank Christie Jilly-Rehak and Matthew Mills and the Stanford Nanocharacterization Laboratory for instrument support on the Cameca NanoSIMS 50L. The Cameca NanoSIMS 50L is supported by the National Science Foundation (ECCS-2026822). Part of this work was performed at the Stanford Nano Shared Facilities (SNSF), supported by the NSF under award ECCS-1542152. Mass spectrometry was performed at the Vincent Coates Foundation Mass Spectrometry Laboratory, Stanford University Mass Spectrometry, supported in part by NIH P30 CA124435 utilizing the Stanford Cancer Institute Proteomics/Mass Spectrometry Shared Resource.

REFERENCES

(1) Munro, S. *Cell* **2003**, *115*, 377−388.
(2) Jacobson, K.; Mouritsen, O. G.; Anderson, R. G. W. *Nat. Cell Biol.* **2007**, *9*, 7−14.
(3) Simons, K.; Toomre, D. *Nat. Rev. Mol. Cell Biol.* **2000**, *1*, 31−39.
(4) Mukherjee, S.; Maxfield, F. R. *Traffic* **2000**, *1*, 203−211.
(5) Goronzy, I. N.; Rawle, R. J.; Boxer, S. G.; Kasson, P. M. *Chem. Sci.* **2018**, *9*, 2340−2347.
(6) Alwarawrah, M.; Dai, J.; Huang, J. *J. Phys. Chem. B* **2010**, *114*, 7516−7523.
(7) de Meyer, F.; Smit, B. *Proc. Natl. Acad. Sci.* **2009**, *106*, 3654−3658.
(8) Róg, T.; Pasenkiewicz-Gierula, M. *FEBS Lett.* **2001**, *502*, 68−71.
(9) Su, Y.; Li, Q.; Chen, L.; Yu, Z. *Colloids Surf., A* **2007**, *293*, 123−129.
(10) Gong, K.; Feng, S.-S.; Go, M. L.; Soew, P. H. *Colloids Surf., A* **2002**, *207*, 113−125.
(11) Li, X.-M.; Momsen, M. M.; Smaby, J. M.; Brockman, H. L.; Brown, R. E. *Biochemistry* **2001**, *40*, 5954−5963.
(12) Mori, K.; Mahmood, M. I.; Neya, S.; Matsuzaki, K.; Hoshino, T. *J. Phys. Chem. B* **2012**, *116*, 5111−5121.
(13) Patel, D. S.; Park, S.; Wu, E. L.; Yeom, M. S.; Widmalm, G.; Klauda, J. B.; Im, W. *Biophys. J.* **2016**, *111*, 1987−1999.
(14) Fujita, A.; Cheng, J.; Hirakawa, M.; Furukawa, K.; Kusunoki, S.; Fujimoto, T. *Mol. Biol. Cell* **2007**, *18*, 2112−2122.
(15) Cebecauer, M.; Hof, M.; Amaro, M. *Biophys. J.* **2017**, *113*, 1194−1199.
(16) Yamamoto, N.; Matsubara, T.; Sato, T.; Yanagisawa, K. *Biochim. Biophys. Acta, Biomembr.* **2008**, *1778*, 2717−2726.
(17) Rabin, S. J.; Mocchetti, I. *J. Neurochem.* **2002**, *65*, 347−354.
(18) Farooqui, T.; Franklin, T.; Pearl, D. K.; Yates, A. J. *J. Neurochem.* **2002**, *68*, 2348−2355.
(19) Hur, J.-Y.; Welander, H.; Behbahani, H.; Aoki, M.; Frånberg, J.; Winblad, B.; Frykman, S.; Tjernberg, L. O. *FEBS J.* **2008**, *275*, 1174−1187.
(20) Foster, L. J.; de Hoog, C. L.; Mann, M. *Proc. Natl. Acad. Sci.* **2003**, *100*, 5813−5818.
(21) Nebl, T.; Pestonjamasp, K. N.; Leszyk, J. D.; Crowley, J. L.; Oh, S. W.; Luna, E. J. *J. Biol. Chem.* **2002**, *277*, 43399−43409.
(22) Nyholm, T. K. M.; Lindroos, D.; Westerlund, B.; Slotte, J. P. *Langmuir* **2011**, *27*, 8339−8350.
(23) Heberle, F. A.; Wu, J.; Goh, S. L.; Petruzielo, R. S.; Feigenson, G. W. *Biophys. J.* **2010**, *99*, 3309−3318.
(24) Zhao, J.; Wu, J.; Heberle, F. A.; Mills, T. T.; Klawitter, P.; Huang, G.; Costanza, G.; Feigenson, G. W. *Biochim. Biophys. Acta, Biomembr.* **2007**, *1768*, 2764−2776.
(25) Veatch, S. L.; Keller, S. L. *Phys. Rev. Lett.* **2005**, *94*, 148101.
(26) Parasassi, T.; De Stasio, G.; d'Ubaldo, A.; Gratton, E. *Biophys. J.* **1990**, *57*, 1179−1186.
(27) Parasassi, T.; Gratton, E. *J. Fluoresc.* **1995**, *5*, 59−69.
(28) Kusumi, A.; Sako, Y.; Yamamoto, M. *Biophys. J.* **1993**, *65*, 2021−2040.
(29) Dietrich, C.; Yang, B.; Fujiwara, T.; Kusumi, A.; Jacobson, K. *Biophys. J.* **2002**, *82*, 274−284.
(30) Marsh, D. *Methods* **2008**, *46*, 83−96.
(31) Elkins, M. R.; Bandara, A.; Pantelopulos, G. A.; Straub, J. E.; Hong, M. *J. Phys. Chem. B* **2021**, *125*, 1825−1837.
(32) Skaug, M. J.; Longo, M. L.; Faller, R. *J. Phys. Chem. B* **2011**, *115*, 8500−8505.
(33) Hughes, L. D.; Rawle, R. J.; Boxer, S. G. *PLoS One* **2014**, *9*, No. e87649.
(34) Schuck, S.; Honsho, M.; Ekroos, K.; Shevchenko, A.; Simons, K. *Proc. Natl. Acad. Sci.* **2003**, *100*, 5795−5800.
(35) London, E.; Brown, D. A. *Biochim. Biophys. Acta, Biomembr.* **2000**, *1508*, 182−195.
(36) Zhao, J.; Wu, J.; Shao, H.; Kong, F.; Jain, N.; Hunt, G.; Feigenson, G. *Biochim. Biophys. Acta, Biomembr.* **2007**, *1768*, 2777−2786.
(37) Eggeling, C.; Ringemann, C.; Medda, R.; Schwarzmann, G.; Sandhoff, K.; Polyakova, S.; Belov, V. N.; Hein, B.; von Middendorff, C.; Schönle, A.; Hell, S. W. *Nature* **2009**, *457*, 1159−1162.
(38) Honigmann, A.; Mueller, V.; Ta, H.; Schoenle, A.; Sezgin, E.; Hell, S. W.; Eggeling, C. *Nat. Commun.* **2014**, *5*, 5412.
(39) Hauri, E. H.; Papineau, D.; Wang, J.; Hillion, F. *Chem. Geol.* **2016**, *420*, 148−161.
(40) Kraft, M. L.; Fishel, S. F.; Marxer, C. G.; Weber, P. K.; Hutcheon, I. D.; Boxer, S. G. *Appl. Surf. Sci.* **2006**, *252*, 6950−6956.
(41) Lozano, M. M.; Liu, Z.; Sunnick, E.; Janshoff, A.; Kumar, K.; Boxer, S. G. *J. Am. Chem. Soc.* **2013**, *135*, 5620−5630.
(42) Moss, F. R.; Boxer, S. G. *J. Am. Chem. Soc.* **2016**, *138*, 16737−16744.
(43) Kraft, M. L.; Weber, P. K.; Longo, M. L.; Hutcheon, I. D.; Boxer, S. G. *Science* **2006**, *313*, 1948−1951.
(44) Konyakhina, T. M.; Wu, J.; Mastroianni, J. D.; Heberle, F. A.; Feigenson, G. W. *Biochim. Biophys. Acta, Biomembr.* **2013**, *1828*, 2204−2214.
(45) Brown, A. C.; Wrenn, S. P. *Langmuir* **2013**, *29*, 9832−9840.
(46) McMahon, G.; Saint-Cyr, H. F.; Lechene, C.; Unkefer, C. J. *J. Am. Soc. Mass Spectrom.* **2006**, *17*, 1181−1187.
(47) Legent, G.; Delaune, A.; Norris, V.; Delcorte, A.; Gibouin, D.; Lefebvre, F.; Misevic, G.; Thellier, M.; Ripoll, C. *J. Phys. Chem. B* **2008**, *112*, 5534−5546.
(48) Boxer, S. G.; Kraft, M. L.; Weber, P. K. *Annu. Rev. Biophys.* **2009**, *38*, 53−74.
(49) Schwarzmann, G.; Sandhoff, K. *Methods Enzymol.* **1987**, *138*, 319−341.
(50) Neuenhofer, S.; Schwarzmann, G.; Egge, H.; Sandhoff, K. *Biochemistry* **1985**, *24*, 525−532.
(51) Rodriguez, N.; Pincet, F.; Cribier, S. *Colloids Surf., B* **2005**, *42*, 125−130.
(52) Reeves, J. P.; Dowben, R. M. *J. Cell. Physiol.* **1969**, *73*, 49−60.
(53) Cremer, P. S.; Boxer, S. G. *J. Phys. Chem. B* **1999**, *103*, 2554−2559.
(54) Hung, W.-C.; Lee, M.-T.; Chen, F.-Y.; Huang, H. W. *Biophys. J.* **2007**, *92*, 3960−3967.
(55) Ma, Y.; Ghosh, S. K.; DiLena, D. A.; Bera, S.; Lurio, L. B.; Parikh, A. N.; Sinha, S. K. *Biophys. J.* **2016**, *110*, 1355−1366.
(56) Pandit, S. A.; Jakobsson, E.; Scott, H. L. *Biophys. J.* **2004**, *87*, 3312−3322.
(57) Javanainen, M.; Martinez-Seara, H.; Vattulainen, I. *Sci. Rep.* **2017**, *7*, 1143.
(58) Sodt, A. J.; Pastor, R. W.; Lyman, E. *Biophys. J.* **2015**, *109*, 948−955.
(59) Shi, J.; Yang, T.; Kataoka, S.; Zhang, Y.; Diaz, A. J.; Cremer, P. S. *J. Am. Chem. Soc.* **2007**, *129*, 5954−5961.
(60) Tachi, Y.; Okamoto, Y.; Okumura, H. *Sci. Rep.* **2019**, *9*, 6853−6863.
(61) Shang, Z.; Mao, Y.; Tero, R.; Liu, X.; Hoshino, T.; Tanaka, M.; Urisu, T. *Chem. Phys. Lett.* **2010**, *497*, 108−114.
(62) Rusnati, M.; Urbinati, C.; Tanghetti, E.; Dell'Era, P.; Lortat-Jacob, H.; Presta, M. *Proc. Natl. Acad. Sci.* **2002**, *99*, 4367−4372.
(63) Nishio, M.; Fukumoto, S.; Furukawa, K.; Ichimura, A.; Miyazaki, H.; Kusunoki, S.; Urano, T.; Furukawa, K. *J. Biol. Chem.* **2004**, *279*, 33368−33378.
(64) Carton, I.; Malinina, L.; Richter, R. P. *Biophys. J.* **2010**, *99*, 2947−2956.
(65) Gu, R.-X.; Ingólfsson, H. I.; de Vries, A. H.; Marrink, S. J.; Tieleman, D. P. *J. Phys. Chem. B* **2017**, *121*, 3262−3275.
(66) Leeb, F.; Maibaum, L. *Biophys. J.* **2018**, *115*, 2179−2188.
(67) Ionova, I. V.; Livshits, V. A.; Marsh, D. *Biophys. J.* **2012**, *102*, 1856−1865.

https://doi.org/10.1021/acs.analchem.2c01336
Anal. Chem. 2022, 94, 9750−9757

Supporting Information For: Recombination Between ^{13}C and ^{2}H to Form Acetylide ($^{13}C_2{}^{2}H^-$) Probes Nanoscale Interactions in Lipid Bilayers Via Dynamic Secondary Ion Mass Spectrometry: Cholesterol and GM_1 Clustering

Dashiel S. Grusky[a], Frank R. Moss III[b], Steven G. Boxer[a,*]

[a] Department of Chemistry, Stanford University, Stanford, CA 94305, USA
[b] Linac Coherent Light Source, SLAC National Accelerator Laboratory, Menlo Park, CA 94025, USA

* Corresponding author: sboxer@stanford.edu

Table of Contents

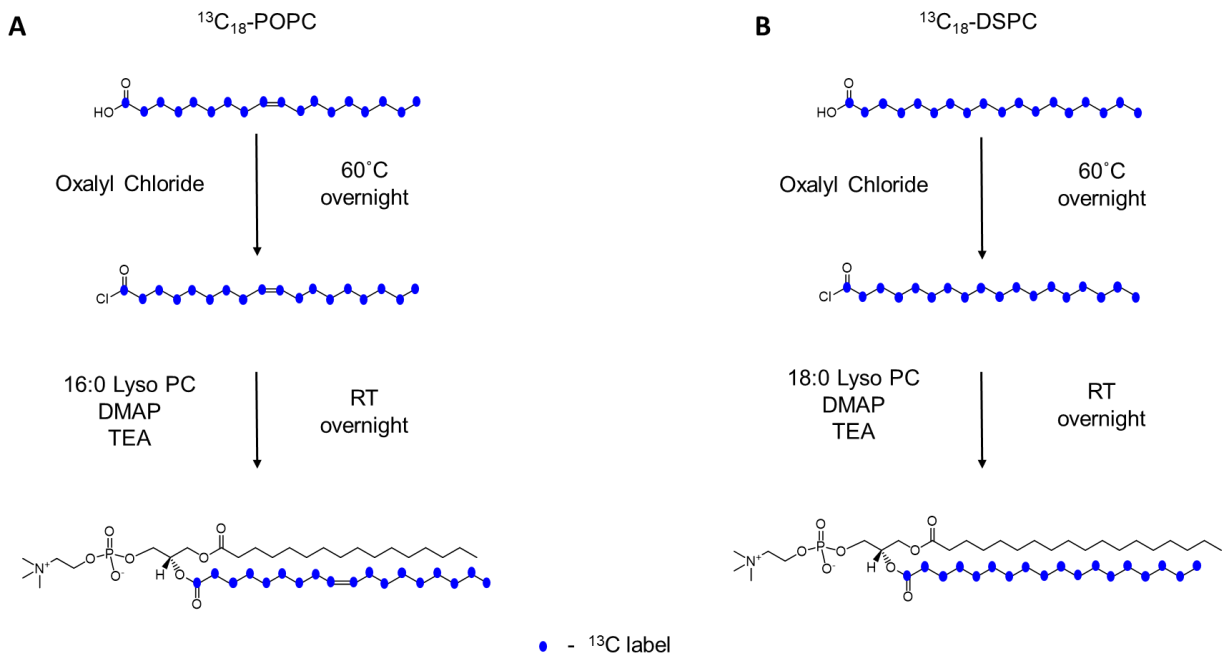

Figure S1. Synthetic scheme for (A) $^{13}C_{18}$-POPC and (B) $^{13}C_{18}$-DSPC[1]

1. Synthesis of $^{13}C_{18}$-POPC and $^{13}C_{18}$-DSPC

Syntheses of $^{13}C_{18}$-POPC and $^{13}C_{18}$-DSPC were carried out as previously described.[1] Both were prepared in a two-step sequence as shown in Figure S1 (schemes a and b, respectively). A flame-dried two-neck 15 mL round bottom flask purged with argon was charged with either $^{13}C_{18}$-stearic acid (49.46 mg, 0.164mM) or $^{13}C_{18}$-oleic acid (50.0 mg, 0.166 mM). Anhydrous toluene (2 mL) was added followed by oxalyl chloride (50 µL, 0.582 mmol). The mixture was left to stir for one hour at room temperature before being placed in a 60˚C oil bath overnight. The resulting mixture was then cooled, and the solvent removed via rotary evaporation. The product was then used without further purification. A flame-dried two-neck 15 mL round bottom flask purged with argon was charged with either 1-stearoyl-2-hydroxy *n*-glycero-3-phosphocholine (116.74mg, 0.223 mmol, for $^{13}C_{18}$-DSPC) or 1-palmitoyl-2-hydroxy *n*-glycero-3-phosphocholine (101.1 mg, 0.204mmol, for $^{13}C_{18}$-POPC) and 4-dimethylaminopyridine (2 mg, 0.016 mmol). Each was then dissolved in anhydrous chloroform (2 mL). Crude $^{13}C_{18}$-stearoyl chloride or $^{13}C_{18}$-oleoyl chloride prepared in the first step was dissolved in anhydrous chloroform (3 mL) and then added to each mixture, followed by anhydrous triethylamine (22.5 µL, 0.161 mmol). The mixture was then stirred overnight at room temperature (RT). Following the evaporation of the solvent, silica gel column chromatography (chloroform:methanol:water 65:25:4) yielded the pure (verified by thin layer chromatography (TLC)) $^{13}C_{18}$-POPC (12.76 mg, 9.9% yield over 2 steps) or $^{13}C_{18}$-DSPC (13.50 mg 10.2% yield over 2 steps).

$^{13}C_{18}$-POPC ESI-MS – $[M+H^+]$ *calcd:* 778.64, *found*: 778.88
$^{13}C_{18}$-DSPC ESI-MS - $[M+H^+]$ *calcd:* 808.64, *found*: 808.94

2. Synthesis of $^{13}C_{18}$ and $^{2}H_{35}$ N-hydroxysuccinimide (NHS) stearate

Either $^{13}C_{18}$-stearic acid or $^{2}H_{35}$-stearic acid (30.1 and 56.4 mg, 0.100 and 0.197 mmol, respectively) was added to N-hydroxysuccinimide (22.4 and 31.4 mg, 0.195 and 0.273 mmol, respectively), along with N,N'-Dicyclohexylcarbodiimide (DCC) (59.4 or 87.4 mg, 0.288 and 0.398 mmol, respectively) to a flame-dried 15 mL round bottom flask under argon. Following the addition of anhydrous dioxane (2.5 and 4 mL respectively), the reaction was stirred at room temperature overnight. Following the removal of the solvent under vacuum, the product was purified via silica gel column chromatography (hexane:ethylether 85:15) to yield pure $^{13}C_{18}$-NHS stearate (26.5 mg, 66.2% yield) or $^{2}H_{35}$-NHS stearate (47.9 mg, 58.3% yield).

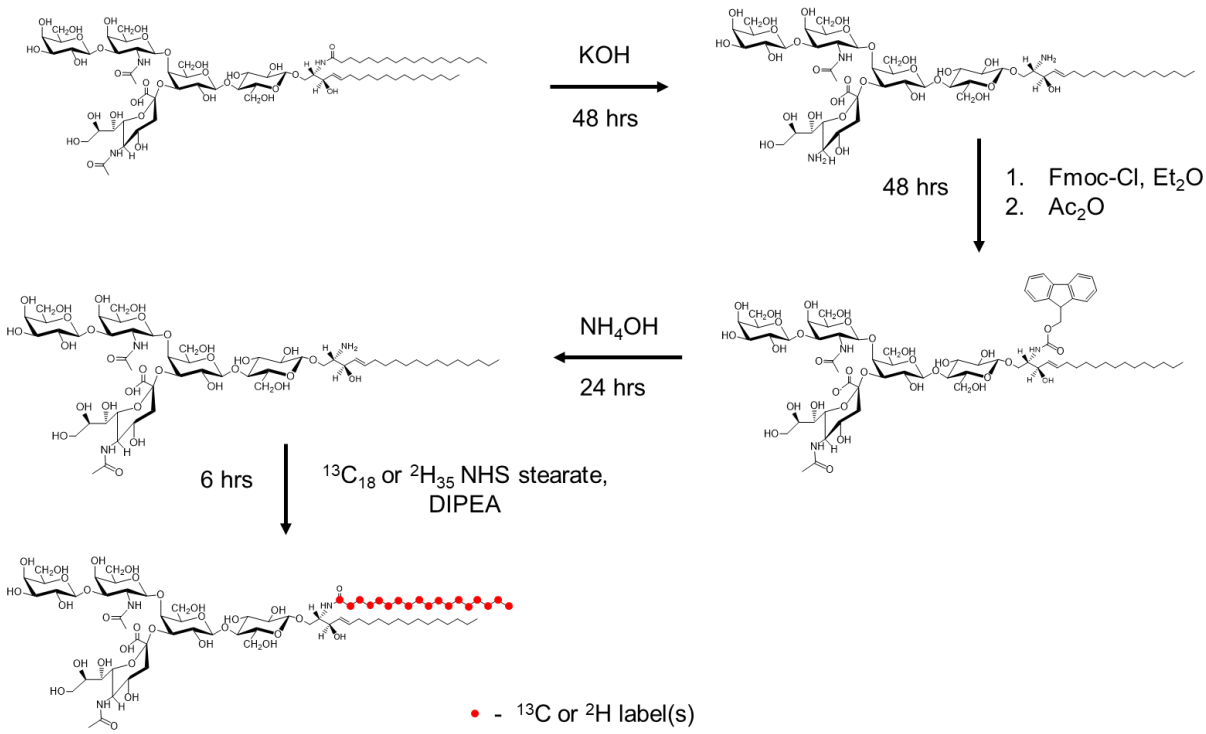

Figure S2. Synthetic scheme for $^{13}C_{18}$-GM_1 and $^{2}H_{35}$-GM_1.[2–4]

3. Synthesis of $^{13}C_{18}$-GM_1 and $^{2}H_{35}$-GM_1

Synthesis of labeled GM_1 was carried out by adapting previously described methods[2,3] to attach ^{13}C- and ^{2}H-labeled NHS stearates to lyso-GM_1. The synthetic scheme is shown in Figure S2. To a solution of 2 M potassium hydroxide in deoxygenated propan-1-ol under argon was added GM_1 (200 mg, 0.137 mmol) dissolved in deoxygenated propan-1-ol. The resulting mixture was stirred for 48 hours at 90˚C. Following the removal of solvent, the crude product was neutralized, and excess salts were removed via dialysis with a Pur-A-Lyzer Mega 1000 dialysis kit (1000 kDa MWCO). Remaining water was then removed via lyophilization and the crude mixture purified via silica gel column chromatography (chloroform:methanol:2.5 M ammonium hydroxide 60:40:9) to yield deacetyl-lyso-GM_1 (28 mg, 17% yield). Deacetyl-lyso-GM_1 (44.4 mg, 0.036 mmol, from multiple first step reactions) was partitioned into a 1:1 mixture of aqueous $NaHCO_3$ (0.1 M) and diethyl ether before being cooled in a -20 ˚C freezer until the aqueous layer froze. Fluorenylmethyloxycarbonyl chloride (Fmoc-Cl) in hexane (11.25 mg, 0.043 mmol in 1.5 mL *n*-hexane) was then added and the mixture stirred at 4 ˚C for 24 hours, or until ESI-MS showed disappearance of the starting material. If starting material remained, additional Fmoc-Cl was added. Acetic anhydride (15 µL, 0.147 mmol) was added and the mixture stirred for an additional 12 hours. Solvent was then removed under vacuum and purified by silica gel column chromatography (isopropanol:hexane:water 55:30:12) to yield pure Fmoc-lyso-GM_1 (21.8 mg, 40.5% yield). N-Fmoc-lyso-GM_1 (47 mg, 0.031 mmol, from multiple previous steps) was then treated with ammonium hydroxide (6 mL) and stirred at room temperature for 12 hours. Solvent was removed via lyophilization and the product purified via silica gel column chromatography (chloroform:methanol:2.5 M ammonium hydroxide 60:40:9) to yield the pure lyso-GM_1 (12.4 mg, 31.3% yield). Either $^{13}C_{18}$-stearic acid (5.17 mg, 0.017mmol) or $^{2}H_{35}$-stearic acid (3.77 mg, 0.012 mmol) was added to lyso-GM_1 (4.84 or 5.83 mg, 0.0038 and 0.0046 mmol, respectively) in a flame-dried 10 mL round bottom flask under argon before being dissolved in anhydrous dimethylformamide (DMF) (0.4 mL). Following the addition of N,N-Diisopropylethylamine (DIPEA) (2.5 µL, 0.014 mmol) the mixture was stirred for 12 hours, and the solvent evaporated under vacuum. The crude product was then purified via silica gel column chromatography (chloroform:methanol:water 65:25:4) to yield pure (verified by TLC) $^{13}C_{18}$-GM_1 or $^{2}H_{35}$-GM_1 (2.55 mg, 44.1% yield and 3.03 mg 42.1% yield respectively).

$^{13}C_{18}$-GM_1 ESI-MS – $[M\text{-}H]^-$ *calcd:* 1563.94, *found*: 1563.11
$^{2}H_{35}$-GM_1 ESI-MS – $[M\text{-}H]^-$ *calcd:* 1581.10, *found*: 1581.12

4. Examining the Lower Limits of Atomic Recombination

Many functionally relevant lipids are present in low concentrations in the plasma membrane. To study interactions between functional lipids at low concentrations, atomic recombination must be sensitive enough to detect nanoscale heterogeneity at such concentrations of labeled lipid. In order to examine how sensitive $^{13}C_2{}^2H^-$ formation is to nanoscale heterogeneity, $\Re(^{13}C_2{}^2H^-)$ was compared between bilayers containing labeled lipids in different domains ($^{13}C_{18}$-POPC – $^{2}H_{70}$-DSPC) to those containing labeled lipids in the same domain ($^{13}C_{18}$-DSPC – $^{2}H_{70}$-DSPC). This was done at variable total label concentration. All samples were prepared with an overall composition of POPC:DSPC:CHOL 37.5:37.5:25 (a mixture with known nanoscale separation)[5] with labeled lipids replacing their respective natural abundance lipids. The results can be seen in Figure S3. The first conclusion to be drawn from the figure is that as label concentration decreases, $\Re(^{13}C_2{}^2H^-)$ also decreases. This is due to an increase in the average distance between the ^{13}C and ^{2}H labeled lipids as they are diluted by their respective unlabeled lipids within the bilayer. This trend can be seen for bilayers containing $^{13}C_{18}$-DSPC and $^{2}H_{70}$-DSPC as well as bilayers containing $^{13}C_{18}$-POPC and $^{2}H_{70}$-DSPC. The second conclusion is that even at low label concentration (2 mole percent ^{13}C-labeled lipid and 2 mole percent ^{2}H-labeled lipid), $\Re(^{13}C_2{}^2H^-)$ is still significantly greater when labels are placed in the same ($^{13}C_{18}$-DSPC – $^{2}H_{70}$-DSPC) nanoscale domain. Therefore, even at 4 mole percent total label, it is still possible to detect nanoscale heterogeneity present in model membranes via the formation of $^{13}C_2{}^2H^-$.

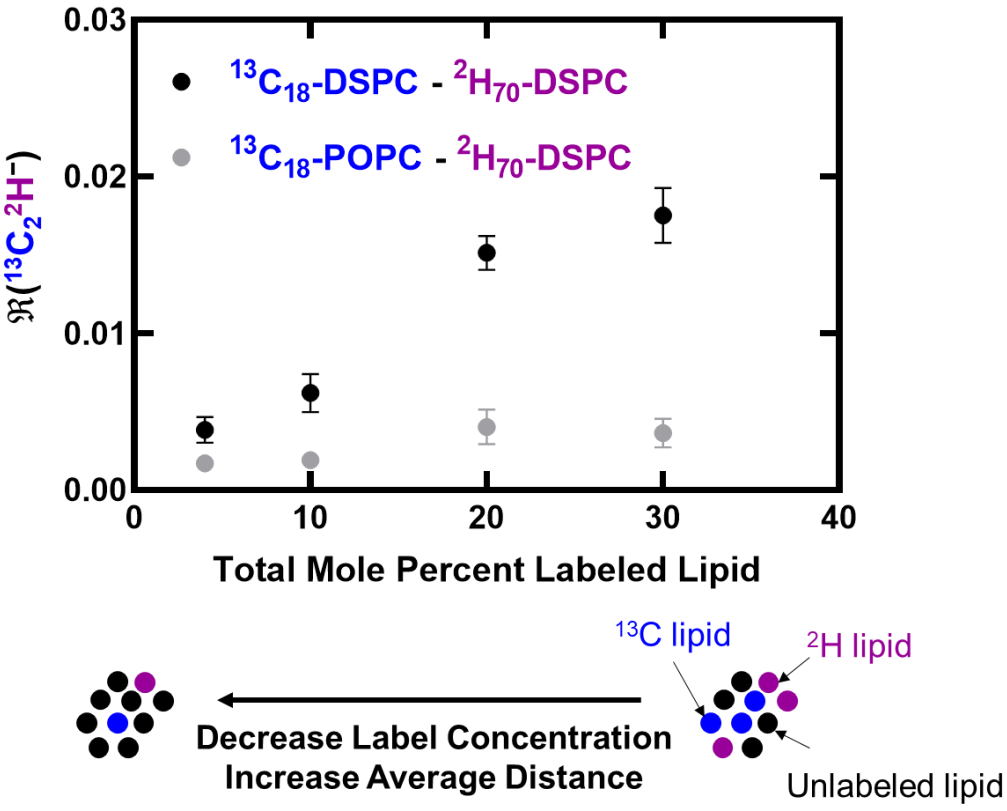

Figure S3. Atomic recombination can detect phase separation at low concentration of labeled lipids. Varying mole percent of labeled lipids were incorporated into lipid mixtures. Total labeled lipid concentration ranged from 30 (15% ^{13}C-labeled lipid and

15% ^{2}H-labeled lipid) to 4 (2% ^{13}C-labeled lipid and 2% ^{2}H-labeled lipid) mole percent. In each case, the labeled lipid replaced the respective natural abundance lipid to maintain an overall composition of DSPC:POPC:CHOL 37.5:37.5:25. As shown in the top-down bilayer schematic below the x axis, this decrease in total ^{13}C- and ^{2}H-labeled lipid concentration results in an increase in the average distance between the differently labeled lipids. As a result, there is a corresponding decrease in $\Re(^{13}C_2{}^{2}H^{-})$ in each labeling regime. $\Re(^{13}C_2{}^{2}H^{-})$ in bilayers containing $^{13}C_{18}$-POPC and $^{2}H_{70}$-DSPC was compared to $\Re(^{13}C_2{}^{2}H^{-})$ in bilayers containing $^{13}C_{18}$-DSPC and $^{2}H_{70}$-DSPC across the range of total labeled lipid concentration. Even with just 4 mole percent of the bilayer labeled, a significant difference in $\Re(^{13}C_2{}^{2}H^{-})$ can be seen between the two labeling schemes. Each point represents the average of six independent bilayer patches.

5. Lipid Compositions

The lipid compositions used for the cholesterol dependence studies are highlighted in Figure S4. The choice of the POPC:DSPC:CHOL composition is based on several factors. Firstly, previous work has shown via FRET that there is nanoscale heterogeneity present within the L_d + L_o and the three-phase-coexistence regions of this mixture.[5] This is reproduced in the work presented here, as none of the compositions examined in Figure 4 displayed any form of resolvable phase separation, either by fluorescence (diffraction limited) or by direct isotope imaging using the NanoSIMS (roughly 50 nm lateral resolution). Secondly, there are well-established protocols in the literature to synthesize isotopically labeled counterparts of the lipids present in this mixture (Sections S1-3 and Figures S1-2). Finally, this mixture is considered a reasonable model for lipids rafts in mammalian cells because it displays nanoscale separation. Since macroscopic separation has not been observed in cells (although it has been observed in giant plasma membrane vesicles[6,7] and yeast vacuoles[8]), nanoscale phase separation may be a better model for lateral heterogeneity in biological systems than microscale phase separation.[9]

Table S1. Composition of samples in Figure 4B-D. Left hand column denotes the cholesterol mole percent of the sample in the corresponding row. Remaining columns denote the composition of mixtures for a given labeling regime. Since POPC and DSPC partition into different nanoscale domains in bilayers, thereby reducing $\Re(^{13}C_2{}^{2}H^{-})$, the label concentration was increased in the $^{13}C_{18}$-DSPC – $^{2}H_{31}$-POPC samples to obtain the highest possible signal and thereby maximize $\Re(^{13}C_2{}^{2}H^{-})$.

Cholesterol Mole Percent	$^{13}C_{18}$-DSPC – $^{2}H_{70}$-DSPC	$^{13}C_{18}$-POPC – $^{2}H_{31}$-POPC	$^{13}C_{18}$-DSPC – $^{2}H_{31}$-POPC
15	POPC: $^{2}H_{70}$-DSPC : $^{13}C_{18}$-DSPC 42.5 : 21.25 : 21.25	$^{13}C_{18}$-POPC: $^{2}H_{31}$-POPC : DSPC 21.25 : 21.25 : 42.5	$^{2}H_{31}$-POPC : $^{13}C_{18}$-DSPC 42.5 : 42.5
20	POPC: $^{2}H_{70}$-DSPC : $^{13}C_{18}$-DSPC 40 : 20 : 20	$^{13}C_{18}$-POPC: $^{2}H_{31}$-POPC : DSPC 20 : 20 : 40	$^{2}H_{31}$-POPC : $^{13}C_{18}$-DSPC 40 : 40
25	POPC: $^{2}H_{70}$-DSPC : $^{13}C_{18}$-DSPC 37.5 : 18.75 : 18.75	$^{13}C_{18}$-POPC: $^{2}H_{31}$-POPC : DSPC 18.75 : 18.75 : 37.5	$^{2}H_{31}$-POPC : $^{13}C_{18}$-DSPC 37.5 : 37.5
30	POPC: $^{2}H_{70}$-DSPC : $^{13}C_{18}$-DSPC 35 : 17.5 : 17.5	$^{13}C_{18}$-POPC: $^{2}H_{31}$-POPC : DSPC 17.5 : 17.5 : 35	$^{2}H_{31}$-POPC : $^{13}C_{18}$-DSPC 35 : 35

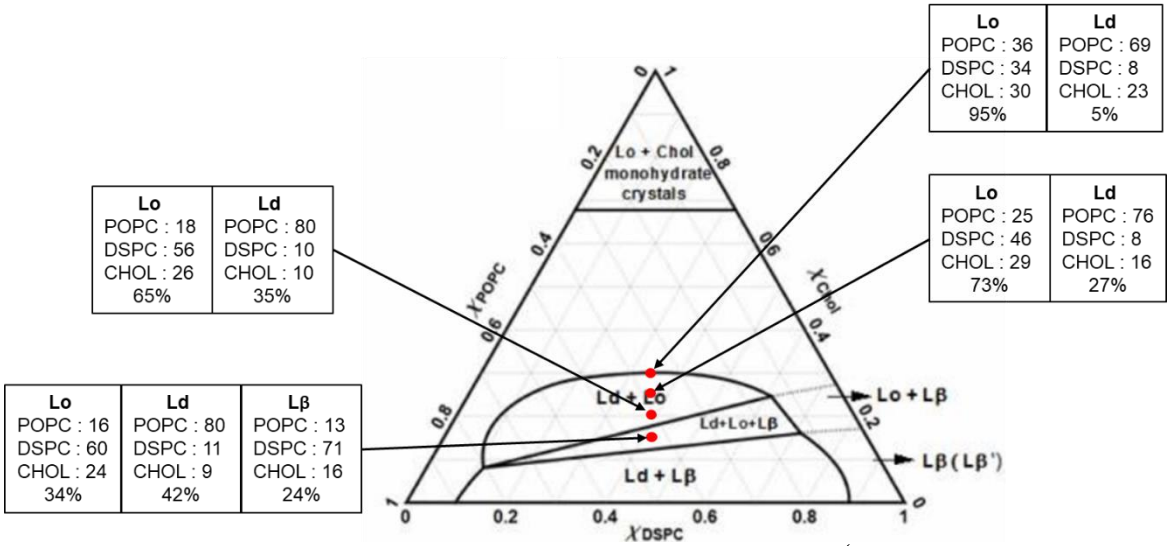

Figure S4. Phase diagram and mixture compositions. Phase diagram adapted from ref. 5 (Konyakhina, T. M.; Wu, J.; Mastroianni, J. D.; Heberle, F. A.; Feigenson, G. W. Phase Diagram of a 4-Component Lipid Mixture: DSPC/DOPC/POPC/Chol. *Biochim. Biophys. Acta BBA - Biomembr.* **2013**, *1828* (9), 2204–2214). Red labels indicate the compositions of the mixtures used for the data shown in Figure 4B-D. The theoretical compositions of and the percent of the bilayer composed by the L_o, L_d and Lβ domains for the indicated points are displayed However, it should be noted that the actual composition of each phase may differ significantly from the theoretical predictions if they do not form ideal mixtures[10–12].

6. Modeling Bilayer Heterogeneity

We further examined whether the phase diagram (Figure S4) alone can explain the trends observed in recombination. This was done by calculating, for a given mixture, how much the composition of each domain deviates from the overall bilayer composition. A mixture whose domain compositions do not deviate at all from the overall bilayer composition is homogenous since there is no difference between the domains and therefore has no separation between components. The more the composition of the domains deviate from the overall mixture, the greater the separation between saturated and unsaturated lipids. The greater the separation, the greater the average DSPC-POPC distance and the smaller the average DSPC-DSPC and POPC-POPC distances. Using this concept, a parameter describing the deviation of a given mixture from complete homogeneity can be calculated as follows:

$$Heterogeneity\ Parameter = \sum_{Lo,Ld,L\beta} (\%\ Domain)\left[\frac{|Domain\ \%\ DSPC - Total\ \%\ DSPC|}{Total\ \%\ DSPC} + \frac{|\ Domain\ \%\ POPC - Total\ \%\ POPC|}{Total\ \%\ POPC} + \frac{|Domain\ \%\ CHOL - Total\ \%\ CHOL|}{Total\ \%\ CHOL}\right]$$

The % Domain refers the percentage of the bilayer composed of the L_o, L_d or L_β phase (for the 30% cholesterol mixture this is 95%, 5% and 0%, respectively). The Domain % DSPC, POPC or CHOL refers the percent of the given domain composed of either DSPC, POPC or cholesterol (for the L_o in the 30% cholesterol mixture this is 36% POPC, 34% DSPC and 30% cholesterol). The Total % DSPC, POPC, and CHOL refers to percent of DSPC, POPC and cholesterol in the whole bilayer (for example, the 30% cholesterol mixture has an overall composition of 35:35:30 DSPC:POPC:CHOL). This calculates how much each domain deviates from the overall mixture and then sums these deviations to get the overall heterogeneity parameter. The larger the parameter, the greater is the deviation from a homogenous bilayer and the greater the separation between saturated and unsaturated lipids. This parameter was calculated for each mixture and plotted in Figure S5. Here it can be seen that as cholesterol concentration increases, the calculated heterogeneity parameter decreases, suggesting that the phase diagram predicts that the bilayer will become

more homogenous as cholesterol concentration increases. Therefore, the diagram suggests that the average DSPC-DSPC and POPC-POPC distances should decrease and the average DSPC-POPC distance should increase as cholesterol concentration increases. This is in contrast to the data presented in Figure 4, which suggests the opposite trend, and therefore the observed recombination trends cannot be explained directly via the phase diagram. We note that modeling intermolecular distances solely from domain compositions does not take into account the different lipid packing in each domain, which does contribute to the measured recombination ratios. We also note that simulations of difference phases could be used to determine average distances, but the results from such simulations would likely depend heavily on the parameters used.

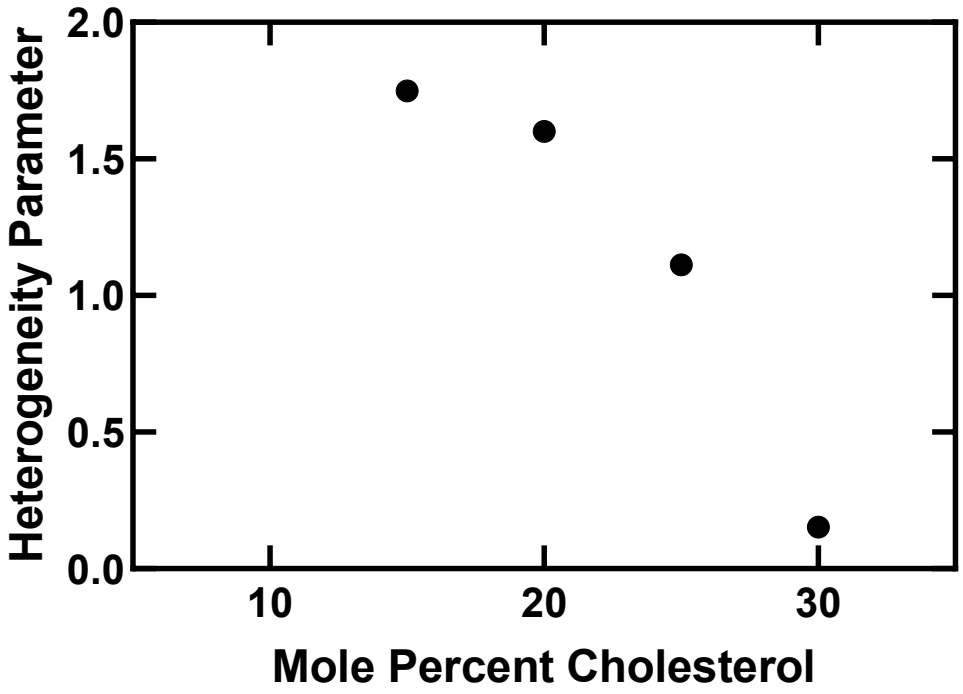

Figure S5. Calculated heterogeneity parameter. The calculated heterogeneity parameter for the mixtures detailed in Table S1 and Figure S4.

7. Optimization of Recombination Signal

The relative concentration of ^{13}C to ^{2}H needed to maximize $\Re(^{13}C_2{}^{2}H^-)$ was investigated. This was done by systematically altering the mole ratio of $^{13}C_{18}$-POPC to $^{2}H_{31}$-POPC from 10:90 to 90:10. The results are shown in Figure S5. It was found that the maximum $\Re(^{13}C_2{}^{2}H^-)$ was attained when labeled lipids were present in a 50:50 ratio. There are many potential factors that could contribute to this being the optimal ratio to incorporate labeled lipids. For instance, at this ratio, the average distance between $^{13}C_{18}$-POPC and $^{2}H_{31}$-POPC should be minimized, which should lead to a high $\Re(^{13}C_2{}^{2}H^-)$. However, since the mechanism behind the formation $^{13}C_2{}^{2}H^-$ is not well-understood, it is possible that other factors, such as ionization efficiency, the presence of covalently

linked ^{13}C labels, and the 2:1 ^{13}C:^{2}H stoichiometry of the acetylide ion may play a role. Regardless, the optimal relative concentration of labeled lipids is shown to be 50:50.

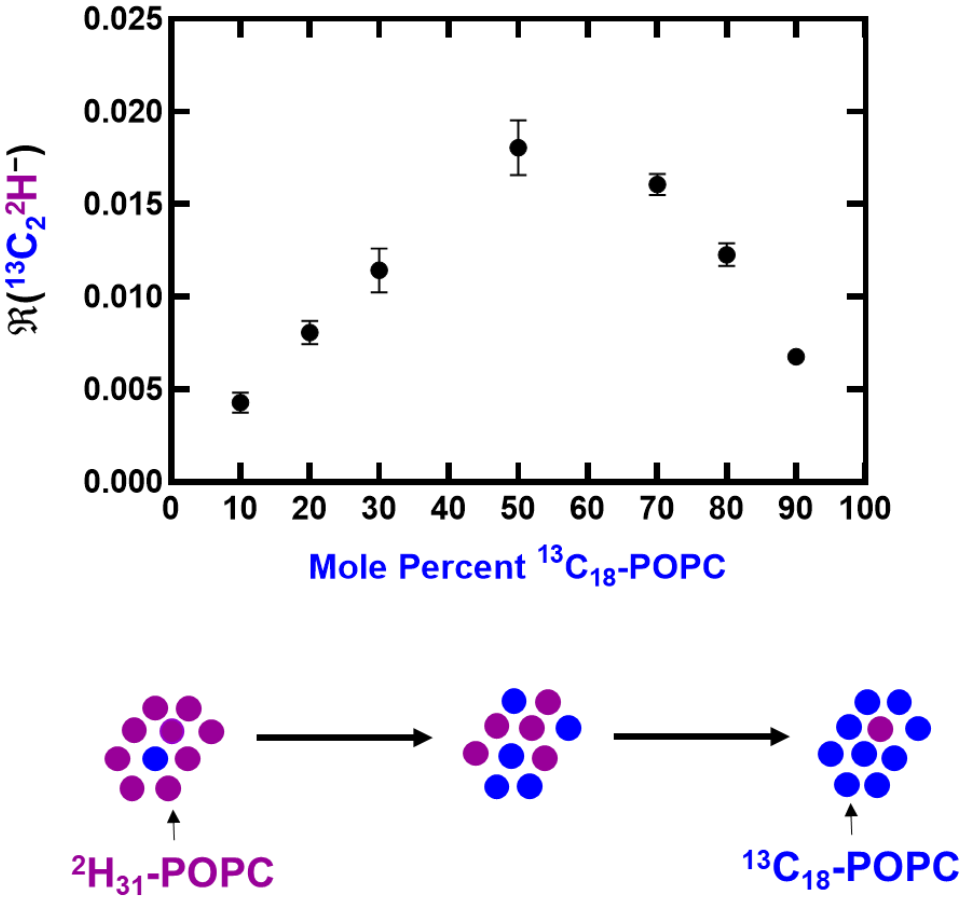

Figure S6. Atomic recombination optimization. The relative amount of $^{13}C_{18}$- and $^{2}H_{31}$-labeled POPC was varied in a homogenous POPC bilayer. The composition is varied from 90:10 $^{2}H_{31}$-POPC:$^{13}C_{18}$-POPC to 10:90 $^{2}H_{31}$-POPC:$^{13}C_{18}$-POPC. This is shown in the top-down schematic of a bilayer below the x-axis. The x-axis tracks the mole percent of $^{13}C_{18}$-POPC in each sample. The remaining mole percent is composed of $^{2}H_{31}$-POPC. Maximum $\Re(^{13}C_2{}^{2}H^-)$ is obtained when ^{13}C- and ^{2}H-labeled lipids are incorporated into bilayers in equal ratios (50:50 $^{13}C_{18}$-POPC:$^{2}H_{31}$-POPC). Each point represents the average of four independent bilayers.

8. Concentration Dependence of Atomic Recombination

Since it has been established that decreasing the total concentration of labeled lipid can in turn lead to a decrease in $\Re(^{13}C_2{}^2H^-)$ (due to an increase in average distance between labels), the implications of this observation on the trend seen in Figure 4D was further investigated. To observe the effect of cholesterol on lipid-lipid interactions while maintaining a constant lipid ratio, labeled POPC and DSPC need to be replaced with cholesterol. If a constant mole percent of the bilayer is labeled, then labeled lipids will be locally concentrated as their natural abundance counterparts are removed from the bilayer and replaced with cholesterol. This is turn will lead to an artificial increase in $\Re(^{13}C_2{}^2H^-)$ (see Figure S8). In order to avoid this, a constant percent of phospholipid in the ordered or disordered domains was labeled for each composition. For instance, in the $^{13}C_{18}$-DSPC – $^{2}H_{31}$-POPC samples shown in Figure 4D, all of the DSPC in the bilayer is $^{13}C_{18}$ labeled and all of the POPC is $^{2}H_{31}$ labeled, so 100% of the phospholipids in the ordered and disordered domains are labeled (Table S1). Since all the phospholipid in the ordered or disordered domain is labeled, and the labels are locally organized, there should not be a decrease in average distance, unless cholesterol impacts lipid-lipid interactions. This effect could either be in the form of diluting labeled lipids, causing the average distance between labels to increase, or increasing the lipid packing, which would decrease the average distance between labels. However, to examine the effect of the decrease in mole percent of labeled lipid, which, in a homogenous sample, would lead to a decrease in average distance and therefore a decrease in $\Re(^{13}C_2{}^2H^-)$, homogenous POPC bilayers with $^{13}C_{18}$-POPC and $^{2}H_{31}$-POPC concentrations identical to the labeled lipid concentrations present in the experiments shown in Figure 4D were examined. Figure S7 shows that as the total label concentration is decreased, $\Re(^{13}C_2{}^2H^-)$ decreases as well and to an extent comparable to that shown in Figure 4D. However, the experiments shown in Figure S7 involve homogenous POPC bilayers, and therefore do not fully capture the complexity of the organization present in the heterogenous bilayers examined in Figure 4. Nevertheless, a conservative estimate would be to assume that the trend shown in Figure 4D is due to the labeling strategy. The decrease in label concentration is not a concern for $^{13}C_{18}$-DSPC - $^{2}H_{70}$-DSPC or $^{13}C_{18}$-POPC - $^{2}H_{31}$-POPC recombination, shown in figure 4B and 4C, as both show a significant increase in $\Re(^{13}C_2{}^2H^-)$ even as label concentration decreases. Attempting to correct for the potential effects of reduced label concentration would only serve to further enhance the observed trends.

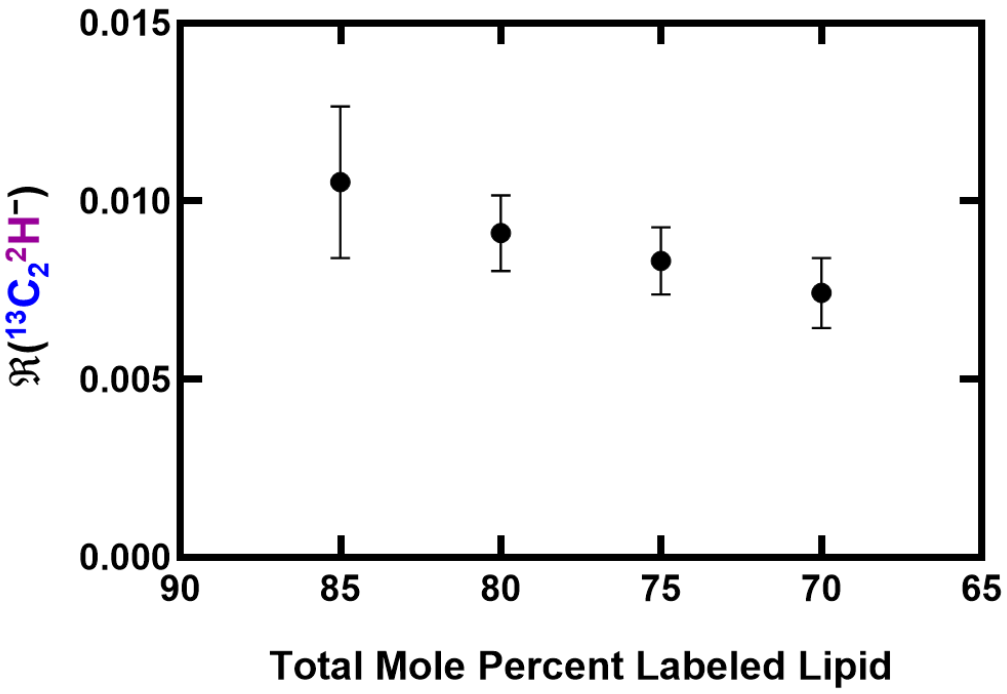

Figure S7. Recombination concentration dependence. Using homogenous POPC bilayers with added $^{13}C_{18}$-POPC and $^{2}H_{31}$-POPC, the total labeled lipid concentration was varied as shown. The total mole percent of labeled lipid was split evenly between

$^{13}C_{18}$- and $^{2}H_{31}$-POPC (for example, at 70 total mole percent labeled lipid, 35 percent is $^{13}C_{18}$-POPC and 35 percent is $^{2}H_{31}$-POPC. The remainder of the bilayer is composed of unlabeled POPC). The resulting recombination ratio decreases as a function of decreasing label concentration, due to labels being father apart on average. Each point represents the average of ten independent bilayers.

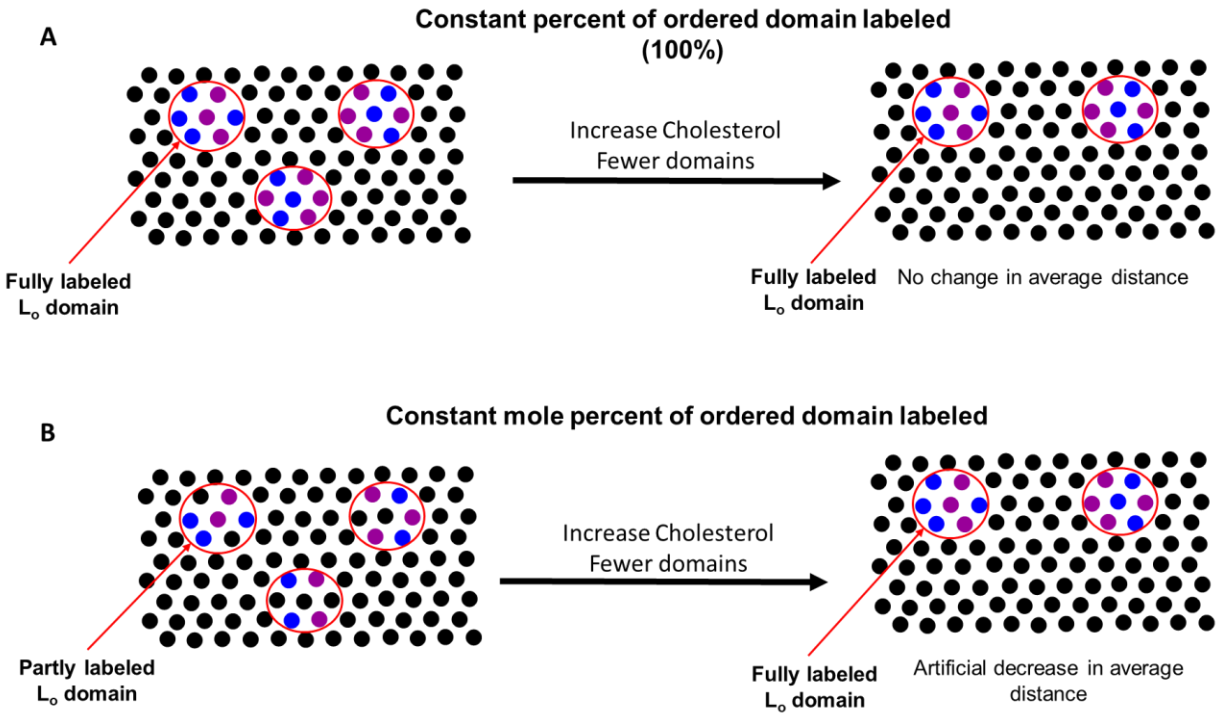

Figure S8. Effect of labeling strategy on average distance between ^{13}C and ^{2}H labels. A top-down view of a lipid bilayer with nanoscale separation. Black circles are unlabeled lipids, blue circles are ^{13}C-labeled lipids and purple are ^{2}H-labeled lipids. The red circles denote the edge of ordered domains. As phospholipid is replaced with cholesterol, (i.e., cholesterol concentration increases), the number of domains decreases. There may also be a slight decrease in size of nanodomains, as cholesterol may decrease line tension in macroscopically separating mixtures.[13] (A) If a constant percent of a domain is labeled, then the average distance between labels does not change due to changing the total mole percent of labeled lipid. While the number of domains likely decreases, the average distance between labeled lipids remains unchanged. Therefore, any change in recombination ratio will represent an effect of cholesterol. (B) If the mole percent of label is kept constant, the total percent of the ordered domain that is labeled increases as cholesterol concentration increases. This effect is due to cholesterol replacing unlabeled saturated phospholipids that would otherwise localize into ordered domains. As a result, the average distance between labels decreases and therefore recombination increases as a result of the labeling strategy.

References:

(1) Kraft, M. L.; Weber, P. K; Longo, M. L.; Hutcheon, I. D.; Boxer, S. G. Phase Separation of Lipid Membranes Analyzed with High-Resolution Secondary Ion Mass Spectrometry. *Science* **2006**, *313* (5795), 1948–1951.

(2) Schwarzmann, G.; Sa, K. Lysogangliosides: Synthesis and Use in Preparing Labeled Gangliosides. *Methods Enzymol.* **1987**, *138*, 319–341.

(3) Neuenhofer, S.; Schwarzmann, G.; Egge, H.; Sandhoff, K. Synthesis of Lysogangliosides. *Biochemistry* **1985**, *24* (2), 525–532.

(4) Lozano, M. M.; Liu, Z.; Sunnick, E.; Janshoff, A.; Kumar, K.; Boxer, S. G. Colocalization of the Ganglioside G_{M1} and Cholesterol Detected by Secondary Ion Mass Spectrometry. *J. Am. Chem. Soc.* **2013**, *135* (15), 5620–5630.

(5) Konyakhina, T. M.; Wu, J.; Mastroianni, J. D.; Heberle, F. A.; Feigenson, G. W. Phase Diagram of a 4-Component Lipid Mixture: DSPC/DOPC/POPC/Chol. *Biochim. Biophys. Acta BBA - Biomembr.* **2013**, *1828* (9), 2204–2214.

(6) Baumgart, T.; Hammond, A. T.; Sengupta, P.; Hess, S. T.; Holowka, D. A.; Baird, B. A.; Webb, W. W. Large-Scale Fluid/Fluid Phase Separation of Proteins and Lipids in Giant Plasma Membrane Vesicles. *Proc. Natl. Acad. Sci.* **2007**, *104* (9), 3165–3170.

(7) Levental, I.; Byfield, F. J.; Chowdhury, P.; Gai, F.; Baumgart, T.; Janmey, P. A. Cholesterol-Dependent Phase Separation in Cell-Derived Giant Plasma-Membrane Vesicles. *Biochem. J.* **2009**, *424* (2), 163–167.

(8) Leveille, C. L.; Cornell, C. E.; Merz, A. J.; Keller, S. L. Yeast cells actively tune their membranes to phase separate at temperatures that scale with growth temperatures. *Proc. Natl. Acad. Sci.* **2022**, *119* (4), e2116007119.

(9) Goh, S. L.; Amazon, J. J.; Feigenson, G. W. Toward a Better Raft Model: Modulated Phases in the Four-Component Bilayer, DSPC/DOPC/POPC/CHOL. *Biophys. J.* **2013**, *104* (4), 853–862.

(10) Sodt, A. J.; Pastor, R. W.; Lyman, E. Hexagonal Substructure and Hydrogen Bonding in Liquid-Ordered Phases Containing Palmitoyl Sphingomyelin. *Biophys. J.* **2015**, *109* (5), 948–955.

(11) Javanainen, M.; Martinez-Seara, H.; Vattulainen, I. Nanoscale Membrane Domain Formation Driven by Cholesterol. *Sci. Rep.* **2017**, *7* (1), 1143.

(12) Pandit, S. A.; Jakobsson, E.; Scott, H. L. Simulation of the Early Stages of Nano-Domain Formation in Mixed Bilayers of Sphingomyelin, Cholesterol, and Dioleylphosphatidylcholine. *Biophys. J.* **2004**, *87* (5), 3312–3322.

(13) Wen-Chyan, T.; Feigenson, G. W. Lowering line tension with high cholesterol content induces a transition from macroscopic to nanoscopic phase domains in model biomembranes. *Biophys. J.* **2019**, *1861* (2), 478-485.